

# The sdA problem – II. Photometric and Spectroscopic Follow-up

Ingrid Pelisoli<sup>1\*</sup>, S. O. Kepler<sup>1</sup>, D. Koester<sup>2</sup>, B. G. Castanheira<sup>3,4</sup>,  
A. D. Romero<sup>1</sup>, L. Fraga<sup>5</sup>

<sup>1</sup>*Instituto de Física, Universidade Federal do Rio Grande do Sul, 91501-900, Porto-Alegre, RS, Brazil*

<sup>2</sup>*Institut für Theoretische Physik und Astrophysik, Universität Kiel, D-24098, Kiel, Germany*

<sup>3</sup>*Baylor University, Waco, TX - 76798, USA*

<sup>4</sup>*Department of Astronomy, University of Texas at Austin, Austin, TX - 78712, USA*

<sup>5</sup>*Laboratório Nacional de Astrofísica LNA/MCTIC, 37504-364, Itajubá, MG, Brazil*

Accepted XXX. Received YYY; in original form ZZZ

## ABSTRACT

Subdwarf A star (sdA) is a spectral classification given to objects showing H-rich spectra and sub-main sequence surface gravities, but effective temperature lower than the zero-age horizontal branch. Their evolutionary origin is an enigma. In this work, we discuss the results of follow-up observations of selected sdAs. We obtained time resolved spectroscopy for 24 objects, and time-series photometry for another 19 objects. For two targets, we report both spectroscopy and photometry observations. We confirm seven objects to be new extremely-low mass white dwarfs (ELMs), one of which is a known eclipsing star. We also find the eighth member of the pulsating ELM class.

**Key words:** subdwarfs – white dwarfs – binaries: general – stars: evolution

## 1 INTRODUCTION

White dwarf stars are the most common outcome of single-star evolution, corresponding to the final observable evolutionary stage of all stars with initial mass below 7–10.6  $M_{\odot}$  (e.g. Woosley & Heger 2015), including the Sun and over 95 per cent of all stars in the Galaxy. Their relative abundance, combined with a simple structure and long cooling timescales, makes them the perfect laboratory for modelling stellar evolution (e.g. Kalirai et al. 2008; Romero et al. 2015), and for population synthesis studies constraining the age and star formation history of different stellar populations (e.g. Liebert et al. 2005; Tremblay et al. 2016; Kilic et al. 2017). About 25 per cent of white dwarfs in the galactic field are known to have a companion (Toonen et al. 2017), therefore white dwarfs have also the potential to put constraints into binary evolution channels.

Short-period binary white dwarfs in particular are potential progenitors of Type Ia (Webbink 1984; Iben & Tutukov 1984) and Ia supernovae (Bildsten et al. 2007). This fact motivated the first surveys for white dwarfs in close binaries (Robinson & Shafter 1987; Foss et al. 1991), which resulted on null detections. The first successful survey was performed by Marsh et al. (1995). They noticed that the catalogue of Bergeron et al. (1992) contained fourteen white dwarfs with spectroscopic mass below

0.45  $M_{\odot}$ , which cannot be formed within a Hubble time without some form of mass-loss enhancement. They were most likely the remnants of mass transfer in post-main-sequence common-envelope binaries. Indeed, Marsh et al. (1995) confirmed five out of the seven stars they probed to be in binaries. More recent studies suggest that the binary fraction of low-mass white dwarfs ( $M \lesssim 0.45 M_{\odot}$ ) is at least 70 per cent (Brown et al. 2011a). Low-mass single systems can be explained by other mass-loss enhancing mechanisms, such as high metallicity (D’Cruz et al. 1996) or supernova stripping (Wang & Han 2009), by mass ejection caused by a massive planet (Nelemans & Tauris 1998), or by merger events (Zhang & Jeffery 2012; Zhang et al. 2017). For the currently known white dwarfs with mass below 0.3  $M_{\odot}$ , the binary fraction seems to be close to 100 per cent (Brown et al. 2016a). These systems are known as extremely-low mass white dwarfs (ELMs).

The ELM Survey (Brown et al. 2010; Kilic et al. 2011; Brown et al. 2012a; Kilic et al. 2012; Brown et al. 2013; Gianninas et al. 2015; Brown et al. 2016a) made large progress in the study of these objects. They have found 88 systems, 76 of which were confirmed to be in binaries, mostly through the analysis of their radial velocity (RV) variations. Seven systems were found to be pulsators, eight show ellipsoidal variations, and two are eclipsing systems (Hermes et al. 2012, 2013b,a; Kilic et al. 2015; Bell et al. 2015; Brown et al. 2016a). The obtained distribution of secondary mass suggests that over 95 per cent of the sys-

\* E-mail: ingrid.pelisoli@ufrgs.br

tems are not Type Ia supernovae progenitors (Brown et al. 2016a). They are, nonetheless, strong gravitational wave sources (Kilic et al. 2012), given that most systems will merge within a Hubble time (Brown et al. 2016b). The gravitational wave radiation of the shortest orbital period systems ( $P \lesssim 1$  h) may be directly detected by upcoming space-based missions such as the Laser Interferometer Space Antenna (LISA). Kilic et al. (2012) found three systems that should clearly be detected by missions like LISA in the first year of operations. Three other systems are above the proposed  $1\text{-}\sigma$  detection limit after one year of observations. Even when not significantly above the detection limit, ELMs are important indicators of what the Galactic foreground may look like for these detectors. Therefore understanding the space density, period distribution, and merger rate of these systems is crucial for interpreting the results of upcoming space-based gravitational wave missions, and for studying the evolution of interacting binary systems.

The target selection of the ELM Survey was initially developed to find B-type hypervelocity stars (see the MMT Hypervelocity Star Survey: Brown et al. 2009, 2012b, 2014), hence it favours the detection of hot ELMs ( $T_{\text{eff}} \gtrsim 12\,000$  K). Cooler objects ( $T_{\text{eff}} \lesssim 10\,000$  K) were targeted by Brown et al. (2012a). Yet, less than 5 per cent of the objects in the ELM Survey show  $T_{\text{eff}} \lesssim 9\,000$  K, while evolutionary models (Althaus et al. 2013; Córscico & Althaus 2014, 2016; Istrate et al. 2016) predict the same amount of time to be spent above and below said  $T_{\text{eff}}$ . Although the uncertainties in residual burning can significantly influence the cooling timescale, it is still expected that 20–50 per cent of the ELMs should show  $T_{\text{eff}} < 9\,000$  K (Brown et al. 2017; Pelisoli et al. 2017). Moreover, the ELM Survey selection criteria also favoured higher  $\log g$  objects. The low- $\log g$  phases happen before the object reaches the white dwarf cooling track (the objects are hence known as pre-ELMs, see e.g. Maxted et al. 2011, 2014) and are relatively quick. However, pre-ELMs are also much brighter. Assuming a spherical distribution, we found in Pelisoli et al. (2017) that there should be about a hundred detected objects with  $\log g = 5 - 6$  for each object with  $\log g = 6 - 7$  in a magnitude-limited survey. Hence there is clearly a missing population of cool, low-mass ELMs yet to be found, as evidenced in Fig. 1.

In an effort to retrieve these missing objects, Kepler et al. (2016) extended their white dwarf catalogue down to  $\log g = 5.5$ , revealing a population of objects which were dubbed subdwarf A stars (sdAs). Their spectra are dominated by hydrogen lines, suggestive of  $T_{\text{eff}} \sim 10\,000$  K and of  $4.75 < \log g < 6.5$ . Brown et al. (2017) suggested they are mainly metal-poor A/F stars in the halo with an overestimated  $\log g$ , given the pure hydrogen grid used to fit these objects in Kepler et al. (2016). However, as we showed in Pelisoli et al. (2018), the addition of metals to the models does not necessarily lower the estimated  $\log g$ . Moreover, we identified the existence of clearly two population within the sdAs, with overlapping but distinct colour distributions, and found that at least 7 per cent of the sdAs are more likely (pre-)ELMs than main sequence stars, given their physical and kinematic parameters. The missing (pre-)ELMs are thus likely within the sdA population.

In this work, we follow up on selected sdAs to probe their binarity with the aim of extending the population of known (pre-)ELMs to all the space of physical parameters

predicted by the evolutionary models. We obtain both time-resolved spectroscopy to search for radial velocity (RV) variations indicating the presence of a close binary companion, and time-series photometry to look for eclipses, ellipsoidal variations, or pulsations typical of ELMs. Extending the sample of known ELMs to cool temperatures and lower masses will allow us to more robustly test the evolutionary models. With a more complete sample, we will also be able to make more reliable predictions as to the contribution of the gravitational wave signals from ELMs to upcoming missions.

## 2 METHODS

### 2.1 Observations

Our observing campaign targeted bright objects with  $T_{\text{eff}}$  and  $\log g$  in the range predicted by the evolutionary models shown in Fig. 1. Targets with high proper motion and/or high radial velocities, and ELM-like colours, yielding high probability of being a (pre-)ELM according to Pelisoli et al. (2018), were prioritized. We have used the proper motions from the GPS1 catalogue (Tian et al. 2017), which contains all but one of the objects analysed here. Consistency checks were done with the Hot Stuff for One Year (HSOY, Altmann et al. 2017) and the UCAC5 (Zacharias et al. 2017) catalogues. We found the proper motions to agree within uncertainties for all the objects studied here. Priority was also given to objects showing radial velocity variations in the subspectra taken by the Sloan Digital Sky Survey (SDSS). We obtained time-resolved spectroscopy for 26 targets. We have also obtained time-series photometry for 21 targets in the vicinity of the instability strip by Tremblay et al. (2015) and Gianninas et al. (2015), which was empirically obtained taking into account 3D corrections to  $T_{\text{eff}}$  and  $\log g$ . The targets are listed in Table 1, as well as their SDSS  $g$  magnitude, proper motion (ppm), distances given a MS or (pre-)ELM radius and velocities in the Galactic rest frame ( $v_{\text{los}}$ ).

We carried out spectroscopy mainly with the Goodman Spectrograph (Clemens et al. 2004) on the 4.1 m Southern Astrophysical Research (SOAR) Telescope. All exposures were taken with a  $1.0''$  slit, and binned by a factor of two in both dimensions. We used a 1200 l/m grating, with a camera angle of  $30.00^\circ$  and grating angle of  $16.30^\circ$ , obtaining a wavelength coverage of 3600–4950 Å with a resolution of  $\sim 2$  Å.

We also obtained spectroscopy with the GMOS spectrographs (Hook et al. 2004; Gimeno et al. 2016) on both Gemini North and Gemini South 8.1 m telescopes. The exposures were taken with a  $0.75''$  slit. As with SOAR, we binned the CCD by a factor of two in both dimensions and used a 1200 l/mm grating. Exposures centred at both 4400 Å and 4450 Å were taken at each semester, to dislocate the position of the two gaps between the CCDs in GMOS, covering wavelengths 3580–5190 Å and 3630–5240 Å, respectively. Our data was partially affected by the bright columns issue developed by GMOS-S CCD2 and CCD3 during September 30, 2016 – February 21, 2017.

Five  $\log g > 5.5$  objects were observed with the medium resolution echelle spectrograph X-shooter (Vernet et al.

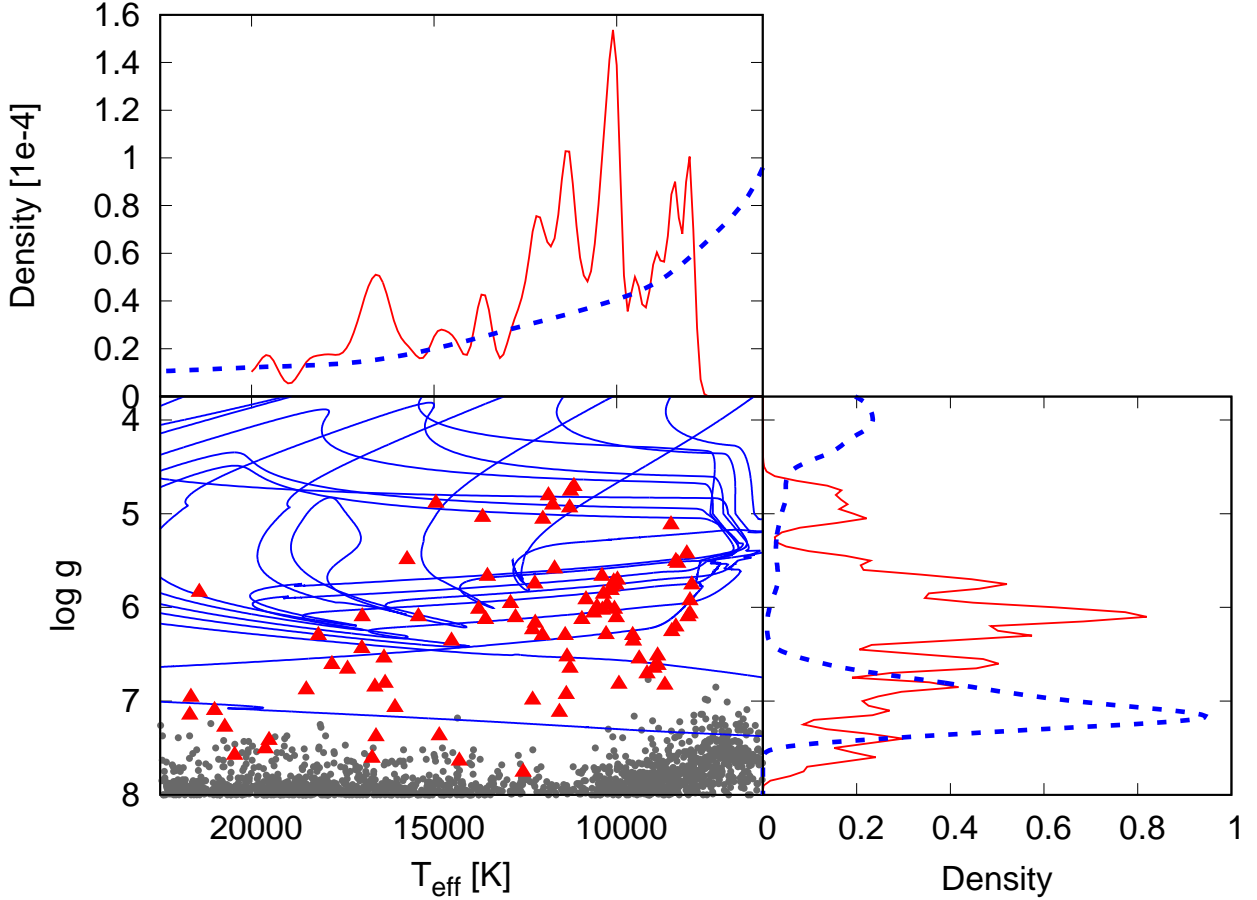


**Figure 1.** Bottom-left panel shows the  $T_{\text{eff}} - \log g$  diagram for the objects in the ELM Survey, shown as red triangles, compared to two binary evolution models of Istrate et al. (2016) (blue lines), resulting on ELMs of masses 0.182 and 0.324  $M_{\odot}$ . The white dwarfs from Kepler et al. (2016) are shown as grey dots for comparison. The top panel shows the distributions in  $T_{\text{eff}}$ , both for the observed ELMs (red continuous line) and obtained from the models (blue dashed line). The bottom-right panel shows the distributions for  $\log g$ . The distributions for the models were obtained taking into account the time spent at each bin of  $T_{\text{eff}}$  or  $\log g$  compared to the total evolutionary time, with a spherical volume correction to account for difference in brightness (see Pelisoli et al. 2018, for further details). Note that there is a lack of known ELMs in the low  $T_{\text{eff}}$  and low  $\log g$  ends of the distribution. There are also missing objects around  $\log g \sim 7.0$ ; however, this range can also be reached through single evolution.

2011), mounted on VLT-UT2 at Paranal, Chile. X-shooter covers the spectral range from the atmospheric cut-off in the UV to the near-infrared with three separate arms: UVB (3000 – 5600 Å), VIS (5600 – 10100 Å) and NIR (10100 – 24000 Å). The data were taken in stare mode, using slits of 1.0", 0.9", and 1.2" for UVB, VIS, and NIR arms, respectively, which allows a resolution of  $\sim 1$  Å. X-shooter has the advantage of also allowing to search for red companions, that could appear as an excess in the NIR arm spectra.

For all instruments, arc-lamp exposures were taken before and after each science exposure to verify the stability. For the wavelength calibration, a CuHeAr lamp was taken after each round of exposures, at the same position of the science frames. Due to the faintness of the objects and the need for multiple spectra, the exposure time was estimated aiming at a median signal-to-noise ratio ( $S/N$ ) of 10–15 per exposure. One radial velocity standard was observed at each semester to verify the reliability of the method, and a spectrophotometric standard star was observed every night for the flux calibration, except for Gemini observa-

tions, which observed one spectrophotometric standard star per semester.

Time-series photometry was obtained with the 1.6 m Perkin-Elmer telescope at Observatório do Pico dos Dias (OPD, Brazil), with an Andor iXon CCD and a red-blocking filter (BG40). We have also used the imaging mode in Goodman at SOAR for photometry, with the S8612 red-blocking filter. The integration time varied from 10 to 30 s, depending on the brightness of the target, with typical readout of 1-3 s.

## 2.2 Data analysis

SOAR spectroscopic data were reduced using IRAF's NOAO package. The frames were first bias-subtracted, and flattened with a quartz lamp flat. We then extracted the spectra and did the wavelength calibration with a CuHeAr lamp spectrum extracted with the same aperture. Finally, flux and extinction calibration were applied. The GEMINI IRAF package was used for data from these telescopes, and the X-shooter

**Table 1.** Followed-up objects and some notable kinematic properties, as well as the SDSS  $g$  magnitude. The first 24 objects were followed-up spectroscopically only, next 19 only photometrically, and the last two both photometrically and spectroscopically. The quoted proper motions are from [Tian et al. \(2017\)](#), except for J110338.46-160617.4, which is not in this catalogue and whose proper motion was then obtained from [Altmann et al. \(2017\)](#). Many objects show unreliable proper motion given the relatively faint ( $g \gtrsim 18$ ) magnitude. Note that most objects would be tens of kpc away given a MS radius.

SDSS J	$g$	ppm (mas/yr)	$\sigma_{\text{ppm}}$ (mas/yr)	$d_{\text{MS}}$ (pc)	$d_{(\text{pre-})\text{ELM}}$ (pc)	$v_{\text{los}}$ (km/s)
004227.73-010634.9	18.63	1.1	2.5	16494	254	111
011508.65+005346.1	18.07	7.5	1.6	16799	232	-173
024932.84-010708.4	19.44	3.2	2.5	27852	405	-146
030608.92-001338.9	16.95	19.3	2.0	6625	108	189
032914.77+003321.8	16.76	11.5	2.3	21652	202	88
045515.00-043231.0	16.49	8.8	2.3	8090	113	64
073934.37+172225.5	18.07	1.4	2.2	10429	173	-65
084034.83+045357.6	17.34	2.7	1.6	9004	140	9
090410.00+034332.9	17.58	3.3	3.1	9697	153	-128
092056.09+013114.8	16.53	12.0	2.1	5346	87	-125
101701.89+070806.8	18.25	6.2	2.9	17876	250	253
112616.66-010140.7	18.50	5.5	2.0	17390	256	62
112620.47+090145.5	18.85	6.2	2.5	23810	331	253
122911.49-003814.4	18.27	10.2	1.8	14079	218	380
142421.30-021425.4	16.93	22.5	1.8	12867	159	14
155937.48+113721.9	17.22	7.4	1.8	30696	270	31
162624.91+162201.5	17.04	6.8	1.8	27991	247	-27
205120.67+014554.4	17.27	9.0	2.4	8954	138	110
213428.63-011409.3	16.96	3.9	2.3	26771	237	142
223831.91+125318.3	15.55	13.6	1.6	3946	61	-18
233343.95-001502.0	19.32	2.2	2.8	26381	382	-16
233403.21+153829.2	16.34	39.1	1.5	3435	62	12
233606.13-102551.5	19.34	5.1	2.7	25693	378	95
233708.62-094307.0	17.90	4.1	1.7	12642	191	-157
045001.34-042712.9	19.07	8.0	3.4	19701	308	-38
073958.57+175834.4	14.75	8.7	2.5	69162	236	-49
075133.48+101809.4	17.40	2.1	2.1	37588	314	-46
075519.92+091511.0	15.32	3.5	1.7	2729	46	-131
075738.94+144827.5	15.04	1.1	1.4	3415	51	-84
092140.37+004347.9	18.39	1.7	2.1	13550	215	-64
094144.89+001233.8	19.28	8.1	2.6	22149	345	-50
104522.80-023735.6	19.28	7.2	2.8	15689	275	101
110338.46-160617.4	15.77	7.3	3.3	5154	75	184
111041.50+132354.3	18.28	19.0	2.4	9648	170	262
112058.97+042012.3	17.87	1.2	2.1	51622	412	158
140353.33+164208.1	16.20	7.7	1.5	5748	85	16
143333.45+041000.8	18.31	2.2	2.3	21349	281	182
160040.95+102511.7	15.00	7.1	1.2	3092	47	94
163625.08+113312.4	17.24	13.0	1.0	12043	164	-215
165700.89+130759.6	15.62	1.5	1.4	4671	68	63
201757.29-125615.6	17.07	4.8	1.7	8796	131	168
204038.41-010215.7	16.59	9.1	1.7	6381	98	165
233625.92+150259.6	17.18	2.6	1.9	9003	134	-160
134336.44+082639.4	16.34	17.5	2.1	5071	81	352
222009.74-092709.9	15.81	9.6	1.6	4659	71	78

pipeline for the VLT data, with equivalent steps in the reduction.

Radial velocity estimates were done with the XCSAO task from the RVSAO package ([Kurtz & Mink 1998](#)), after verifying that the intercalated HeAr lamps presented no shift, which was always the case. We cross-correlated the spectral region covering all visible Balmer lines (typically from 3750 to 4900 Å) to spectral templates from the updated model grid based on [Koester \(2010\)](#), described in [Pelisoli et al. \(2018\)](#). The values of RV were corrected to the Solar System

barycentre given the time of observations and the telescope location. All our RV estimates are given in Table A1. We have not added the RV estimated from the SDSS spectra to our dataset, because it was obtained eight years before our data even in the best of cases, hence the phase might not be accurate to our recently obtained data.

We performed a Shapiro-Wilk normality test ([Shapiro & Wilk 1965](#)) to verify whether the obtained velocities displayed a behaviour which could be explained by Gaussian uncertainties. Next, we calculated the Lomb-



Scargle periodogram (Lomb 1976; Scargle 1982) using the NASA Exoplanet Archive tool<sup>1</sup>. For each of the highest fifty peaks in the periodogram, we calculated an orbital solution of the form

$$RV(t) = RV_0 + K \sin(2\pi t/T + \phi), \quad (1)$$

where  $RV_0$  is the systemic velocity,  $K$  is the semi-amplitude of the RV variation,  $T$  is the period, and  $\phi$  the phase. We selected as the best solution the one with the highest reduced  $R^2$ , defined as

$$R^2 \equiv 1 - \frac{\sum_i (y_i - f_i)^2}{\sum_i (y_i - \bar{y})^2}, \quad (2)$$

where  $y_i$  are the observed values,  $\bar{y}$  is their mean, and  $f_i$  are the adjusted values. This is equivalent to selecting the solution with the smallest reduced  $\chi^2$ .

Each individual spectrum was later Doppler-corrected considering the estimated velocities, and all spectra of each object were combined to obtain a  $S/N \gtrsim 30$  spectrum (the average for the whole sample was  $S/R = 45$ ). Considering the lack of strong metal lines, we fit these spectra to a grid of models assuming metallicity  $Z = 0.1 Z_\odot$ , with the same input physics as described in Pelisoli et al. (2018). We caution that quoted uncertainties are formal fitting errors, and the systematic uncertainties are larger. We previously estimated it to be  $\sim 5$  per cent in  $T_{\text{eff}}$  and 0.25 dex in  $\log g$  (e.g. Pelisoli et al. 2018); however, as we will show in Section 3.4, it seems that the systematic uncertainty in  $\log g$  can actually be higher in the  $T_{\text{eff}} - \log g$  region of the sdAs, and reach 0.5 dex. The SDSS spectra of all objects were also fit to the same  $Z = 0.1 Z_\odot$  grid to allow a comparison. We have relied on the SDSS colours to choose between hot and cool solutions with similar  $\chi^2$ , that arise due to similar equivalent width being possible with different combinations of  $T_{\text{eff}}$  and  $\log g$ . To estimate the mass of each object, we interpolated the models of Althaus et al. (2013). The models of Istrate et al. (2016) made a large improvement to the input physics, by taking into rotational mixing, which was shown to be an important factor in the atmosphere abundances for ELMs. However, the lowest ELM mass in the models of Istrate et al. (2016) is  $0.16 - 0.18 M_\odot$ , depending on the metallicity, and most of our objects show mass lower than that. Only one object (SDSSJ1626+2622) could have its mass accurately determined with Istrate et al. (2016) models, and it agreed with the mass estimate using Althaus et al. (2013) within uncertainties. Hence, to be consistent, we used the models of Althaus et al. (2013) for all mass estimates.

All photometry images were bias-subtracted, and flat-field corrected using dome flats. Aperture photometry was done using the DAOPHOT package in IRAF. A neighbouring non-variable star of similar brightness was used to perform differential photometry. The resulting light curve was analysed with PERIOD04 (Lenz & Breger 2005), in search of pulsations with amplitude at least four times larger than the average amplitude of the Fourier transform. PERIOD04 was also used to fit the light curve and perform pre-whitening when pulsations were found, and to estimate uncertainties using the Monte Carlo method with a 1000 simulations.

### 3 RESULTS

We found seven objects whose RV variations indicate they are in close binaries. They show p-value smaller than 0.15 for the Shapiro-Wilk test, implying that the variations cannot be explained by Gaussian noise to a confidence level of 85 per cent. For six objects out of these seven, the p-value is smaller than 0.05, hence the confidence level is 95 per cent. The orbital solution shows  $R^2$  larger than 0.95 for all but one object.  $T_{\text{eff}}$  and  $\log g$  suggest they are new (pre-)ELMs (see Fig. 27). Their properties are given in Section 3.1.

For six other objects, the p-value is larger than 0.15, but we obtain an orbital solution with a short period ( $P \lesssim 10$  h), expected from (pre-)ELMs in the range of physical parameters for the sdAs (Brown et al. 2017), and  $R^2 \gtrsim 0.85$ . Two other objects shows  $p < 0.05$ , but its atmospheric parameters are compatible with both a pre-ELM and a main sequence star. More data is required to confirm the nature of these eight objects; given the distance modules or proper motion and the estimated physical parameters, we assume they are probable (pre-)ELMs and discuss their properties in Section 3.2.

Six other objects have twelve measurements or more (the average necessary to confirm binary, according to Brown et al. 2016a), in at least three different epochs and often multiple telescopes, but the Shapiro-Wilk test suggested no real variation. These objects are possibly single stars, or show either very short ( $\lesssim 1.0$  h) or long periods ( $\gtrsim 200$  days). We also found no RV variation or red companions for the five objects observed with X-shooter in three nights over a week. All these objects are detailed in Section 3.3.

In Section 3.4, we compare the values of  $T_{\text{eff}}$  and  $\log g$  obtained fitting the SDSS spectra and the SOAR or X-shooter spectra for each object. We were unable to obtain a good fit to the Gemini spectra. The Gemini reduction package interpolates between the CCD gaps before performing the flux calibration, and that seems to be affecting the output to a point where our models cannot fit the slope of the continuum.

In addition, we have found seven new pulsators among the sdAs. For other fourteen observed stars, we have obtained a detection limit  $\lesssim 10$  mmag and found no pulsations. The photometry results are discussed in Section 3.5.

#### 3.1 New (pre-)ELMs

##### 3.1.1 J032914.77+003321.8

The thirty RV estimates for J0329+0033, taken over seven non-consecutive nights at SOAR, yielded a Shapiro-Wilk p-value of 0.004, suggesting with a very high confidence level that the observed variations are not due to chance. We have estimated the period to be  $20.1 \pm 0.1$  h. The semi-amplitude is not well constrained by our data; we estimated it to be  $83 \pm 22$  km s<sup>-1</sup>. This results on an orbital fit with  $R^2 = 0.78$ , shown in Fig. 2, the lowest  $R^2$  among our fits. However, when we assume a main sequence radius, the photometric parallax gives a distance larger than 20 kpc for this object, what is inconsistency with its proper motion of  $11.5 \pm 2.3$  mas yr<sup>-1</sup> (Tian et al. 2017). The systemic velocity is also relatively high,  $153.3 \pm 18$  km s<sup>-1</sup>. Assuming an ELM

<sup>1</sup> <https://exoplanetarchive.ipac.caltech.edu/cgi-bin/Pgram/nph-pgrams>, the distance drops to  $\sim 200$  pc.

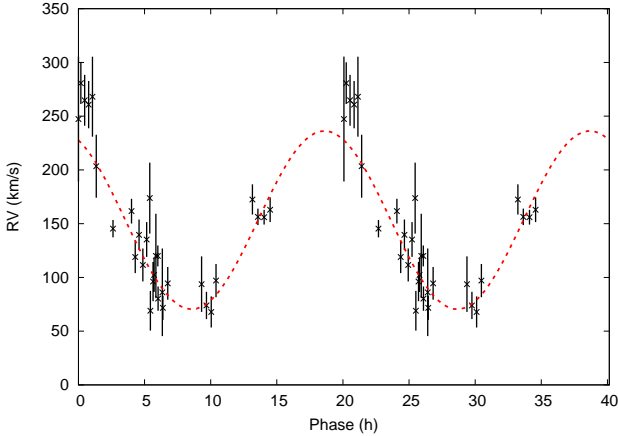


**Figure 2.** Orbital solution for SDSS J032914.77+003321.8, phase-folded to the 20.1 h period. Note that in this and also in the next orbital solution plots, two cycles are shown. The semi-amplitude is  $83 \pm 22 \text{ km s}^{-1}$ , and the systemic velocity is  $153 \pm 18 \text{ km s}^{-1}$ .

Our fit to the SOAR spectrum of J0329+0033 gives  $T_{\text{eff}} = 9080 \pm 10 \text{ K}$  and  $\log g = 5.18 \pm 0.03$ . Interpolating the models of Althaus et al. (2013), we obtain  $M = 0.1536 \pm 0.0006 M_{\odot}$ . Given this mass and the orbital parameters, the minimal mass of the companion (for an edge-on orbit) is  $M_2 = 0.17 M_{\odot}$ , implying a merging time shorter than 765 Gyr.

### 3.1.2 J073934.37+172225.5

We obtained nine spectra in three nights with SOAR for J0739+1722, whose RV variability was already suggested by its SDSS subspectra. The RV estimates from the SOAR spectra give  $p = 0.1465$ . We obtained a period of  $6.64 \pm 0.03 \text{ h}$ , too short for a main sequence star in the sdA range of parameters (Brown et al. 2017), and  $K = 82.6 \pm 6.8 \text{ km s}^{-1}$ . The orbital solution, shown in Fig 3, has a high  $R^2$  of 0.96.

We estimated the mass of the ELM primary to be  $0.145 \pm 0.001 M_{\odot}$ , given the  $T_{\text{eff}} = 7550 \pm 12 \text{ K}$  and the  $\log g = 5.06 \pm 0.05$  estimated from the SOAR combined spectrum. The minimum mass of the companion is  $M_2 = 0.10 M_{\odot}$ . For the mean inclination angle for a random stellar sample,  $i = 60$ , the mass is  $0.12 M_{\odot}$ . Given the orbital parameters, the merging time is smaller than 68 Gyr.

### 3.1.3 J084034.83+045357.6

J0840+0453 was observed in three nights with SOAR, and we obtained nine spectra. A possible RV variability was first detected in the SDSS subspectra. The Shapiro-Wilk test performed in the SOAR RV data confirmed the variability. The best orbital solution (Fig. 4) gives  $R^2 = 0.98$ , with a semi-amplitude of  $221.6 \pm 12.8 \text{ km s}^{-1}$  and a period of  $8.13 \pm 0.01 \text{ h}$ .

Our fit to the SOAR spectra of J0840+0453 gives  $T_{\text{eff}} = 7890 \pm 32 \text{ K}$  and  $\log g = 5.07 \pm 0.09$ , implying an ELM mass of  $M = 0.147 \pm 0.002 M_{\odot}$ . The secondary mass is  $M_2 > 0.59 M_{\odot}$ , hence it is probably a canonical mass white dwarf. The merging time due to gravitational wave radiation is  $\leq 28 \text{ Gyr}$ .

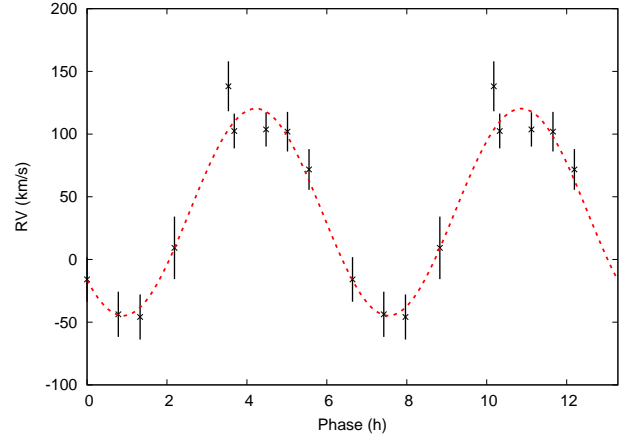


**Figure 3.** Our orbital fit for J073934.37+172225.5, given the SOAR RV estimates. We obtained  $T = 6.61 \pm 0.01 \text{ h}$ ,  $K = 82.6 \pm 6.8 \text{ km s}^{-1}$ ,  $RV_0 = 37.8 \pm 3.4 \text{ km s}^{-1}$ , and  $R^2 = 0.96$ .

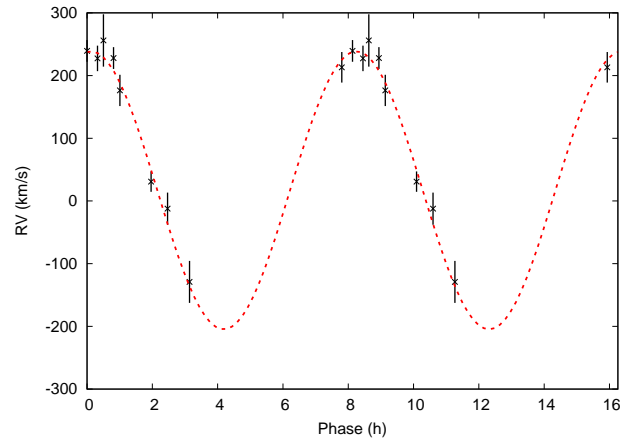


**Figure 4.** The orbital solution for J084034.83+045357.6, a  $0.147 M_{\odot}$  pre-ELM with  $T_{\text{eff}} \sim 8000 \text{ K}$ . The RV estimates are phase-folded to the 8.13 h period, and show a semi-amplitude of  $K = 221.6 \pm 12.8 \text{ km s}^{-1}$  and  $RV_0 = 17 \pm 13 \text{ km s}^{-1}$ .

### 3.1.4 J134336.44+082639.4

J1343+0826 was found to be photometrically variable in our observations carried out with OPD (see Fig. 5), and most likely ELM by Pelisoli et al. (2018). We found a photometric period of about one hour, with an amplitude of  $26.2 \pm 2.3 \text{ mmag}$ . This is consistent with the predicted values of Córscico & Althaus (2016). Unfortunately, this is the only detected period, and therefore we cannot obtain an asteroseismological fit to this object. Spectroscopic follow-up was obtained over five nights at SOAR; twenty-eight spectra were obtained. The derived velocities give  $p = 0.004$ , indicating variability with a high confidence level ( $> 99$  per cent). The dominant period was  $\sim 24 \text{ h}$ , a probable alias given that four of the observed nights consisted of two sets of consecutive nights. A similar  $R^2$  (only 0.5 per cent smaller) is obtained with  $T = 21.39 \pm 0.01 \text{ h}$ , which is the period we adopt for the orbital solution shown in Fig. 6. The derived semi-amplitude is  $136.2 \pm 7.0 \text{ km s}^{-1}$ . The systemic velocity is remarkably high,  $RV_0 = 326.0 \pm 7.2 \text{ km s}^{-1}$ . If

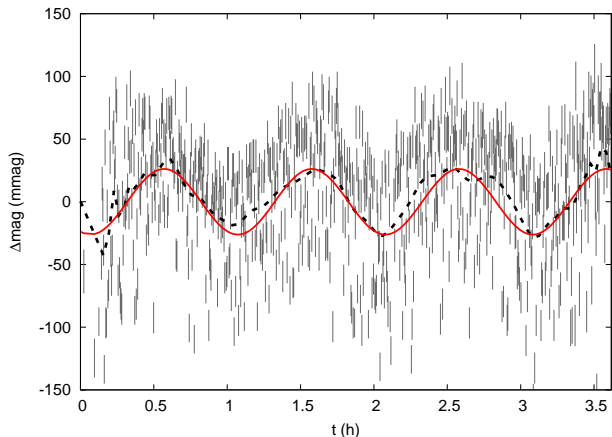


**Figure 5.** The light curve for SDSS J134336.44+082639.4, obtained at OPD. There is a lot of spread in the data due to the variation of the seeing throughout the night. The dashed black line shows the smoothed data. The red line shows the best fit obtained with PERIOD04, with a period of  $3618 \pm 55$  s and amplitude of  $26.1 \pm 2.4$  mmag.

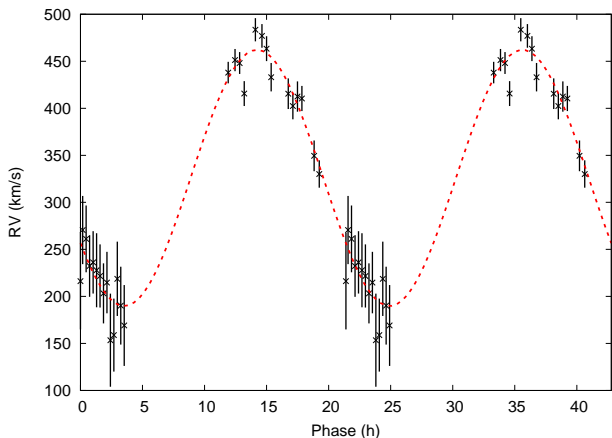


**Figure 6.** Orbital solution for the photometric variable star SDSS J134336.44+082639.4, with  $T = 21.39 \pm 0.01$  h,  $K = 136.2 \pm 7.0$  km s $^{-1}$ ,  $RV_0 = 326.0 \pm 7.2$  km s $^{-1}$ , and  $R^2 = 0.95$ .

the 24.7 h period is the true one, the amplitude would be  $175.5 \pm 6.8$  km s $^{-1}$ , and  $RV_0 = 323.0 \pm 3.8$  km s $^{-1}$ .

The  $\log g$  we estimated from its SOAR spectrum is among the highest in our sample ( $5.97 \pm 0.03$ ), and the effective temperature is nonetheless quite low ( $T_{\text{eff}} = 8120 \pm 10$  K), making it a very interesting addition to the known population of pulsating ELMs. We estimate its mass to be  $M = 0.153 \pm 0.001 M_{\odot}$ , while the companion has  $M_2 > 0.43 M_{\odot}$ . The objects will merge in less than 449 Gyr.

### 3.1.5 J142421.30-021425.4

We followed-up on J1424-0214 given the RV variability suggested by its SDSS subspectra. We observed it in three nights at SOAR, obtaining ten spectra. We obtained a period of  $6.3 \pm 0.4$  h, with a semi-amplitude of  $79.7 \pm 21.8$  km s $^{-1}$ . The orbital solution, shown in Fig. 7, has  $R^2 = 0.988$ .

We derived  $T_{\text{eff}} = 9300 \pm 11$  K and  $\log g = 5.13 \pm$

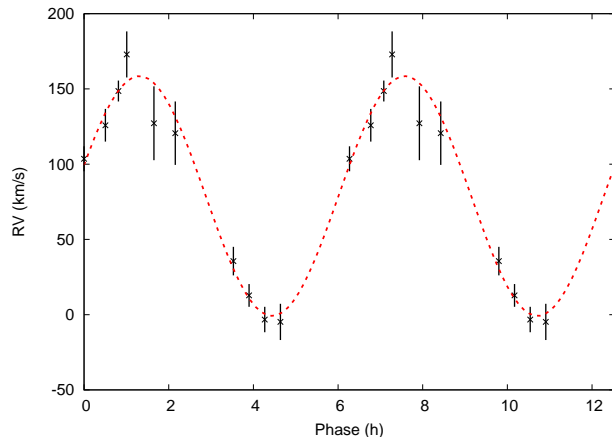


**Figure 7.** The orbital solution obtained for SDSS J142421.30-021425.4, whose RV estimates indicated variability at the 85 per cent confidence level.

0.03 from the SOAR combined spectrum assuming one tenth of the solar metallicity, obtaining  $M = 0.1558 \pm 0.0008 M_{\odot}$  from the evolutionary models of Althaus et al. (2013). Slightly smaller atmospheric parameters are obtained from the SDSS spectrum,  $T_{\text{eff}} = 9090 \pm 24$  K and  $\log g = 4.53 \pm 0.04$ , resulting on  $M = 0.170 \pm 0.002 M_{\odot}$ . Given the estimated period and semi-amplitude, and assuming the parameters derived from the SOAR spectrum are correct, the companion has  $M_2 < 0.09 M_{\odot}$  ( $M_2 = 0.12 M_{\odot}$  for  $q = 60^\circ$ ) and the objects will merge in less than 57 Gyr.

### 3.1.6 J205120.67+014554.4

J2051+0145 would be at a distance of  $\sim 9$  kpc if it had a main sequence radius; however, the estimated proper motion of  $9.0 \pm 2.4$  mas yr $^{-1}$  suggests a smaller distance, compatible with a (pre-)ELM radius. Observing it for five nights at SOAR, and three nights at Gemini South, we obtained twenty-eight spectra. After obtaining a  $p$ -value of only 0.002 (confidence level  $> 99$  per cent), we estimated the period to be  $22.9 \pm 0.2$  h. The semi-amplitude of the orbital solution is  $137.5 \pm 14.0$  km s $^{-1}$ , and the systemic velocity is  $RV_0 = 30.9 \pm 14.1$  km s $^{-1}$ . The orbital solution is shown in Fig. 8.

The estimates of  $T_{\text{eff}}$  and  $\log g$  using the combined SOAR spectrum,  $7810 \pm 13$  K and  $5.00 \pm 0.05$ , give  $M = 0.148 \pm 0.001 M_{\odot}$ . The minimal mass of the secondary is  $M_2 = 0.45 M_{\odot}$ , and the merging time due to the emission of gravitational waves is shorter than 533 Gyr.

### 3.1.7 J092056.09+013114.8 – An eclipsing binary

J0920+0131 is an eclipsing binary identified independently by Palaversa et al. (2013) and Drake et al. (2014). Using data from the the Catalina Real-Time Transient Survey (CRTS, Drake et al. 2009), we estimate the orbital period to be  $15.742 \pm 0.003$  h. The phase-folded light curve is shown in Fig. 9. We obtained thirteen spectra in five nights at SOAR. Fixing the period to the photometric estimate, we obtain an orbital solution with  $R^2 = 0.95$  (see Fig. 10) and  $K = 75.7 \pm 11.5$  km s $^{-1}$ .

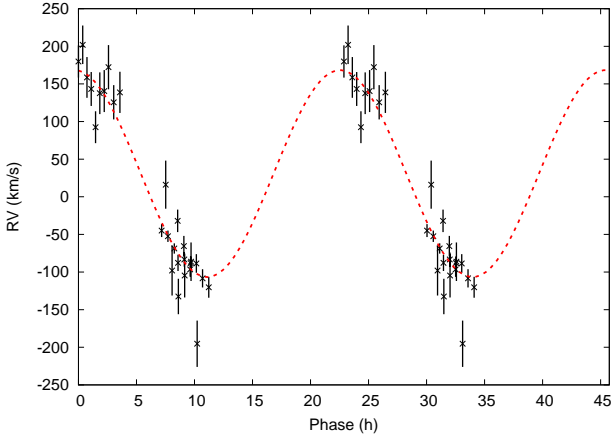


**Figure 8.** Estimated RVs and orbital solution for SDSS J205120.67+014554.4, that was observed with both SOAR and Gemini. The orbital fit gives  $R^2 = 0.93$ .

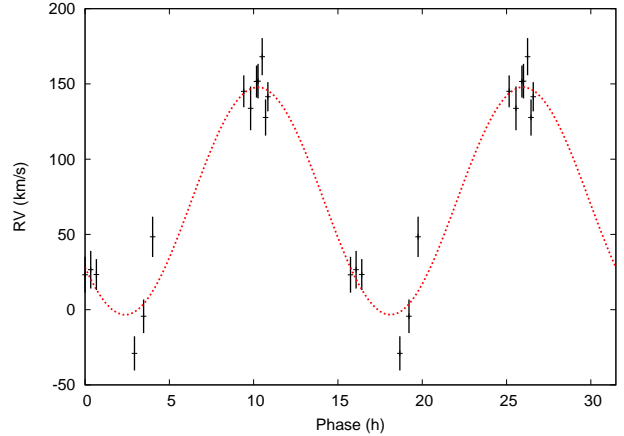


**Figure 10.** RV data and the obtained orbital solution for SDSS J092056.09+013114.8. The RV data are phase-folded to the photometric 15.7 h period.

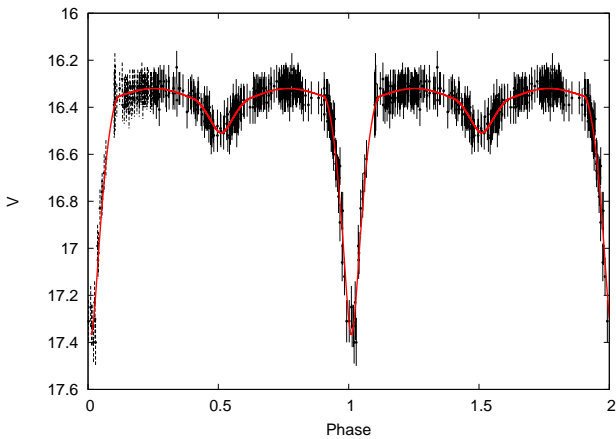


**Figure 9.** Light curve of J0920+0131, phase-folded to the 15.7 h period. The best fit to the light curve, calculated with JKTEBOP, is shown as a red line.

We fit the photometry using JKTEBOP (Southworth et al. 2004), and obtain an orbital inclination of  $82.7 \pm 0.4$  and  $R_2/R_1 = 0.80 \pm 0.03$ . Given this inclination, we obtain  $M_2/M_1 = 0.894$  from the RV fit. Our spectroscopic fit to the spectrum of the primary gives  $T_{\text{eff}} = 7480 \pm 13$  K and  $\log g = 4.80 \pm 0.06$ , implying  $M_1 = 0.149 \pm 0.002 M_{\odot}$  and  $R_1 = 0.25 R_{\odot}$ . Therefore the secondary mass seems to be an even lower mass ELM with  $M_2 = 0.133 \pm 0.002 M_{\odot}$  and  $R_2 = 0.20 R_{\odot}$ . The external uncertainty in the radius, given the 0.25 dex uncertainty in  $\log g$ , is about  $0.7 R_{\odot}$  (assuming a fixed mass of  $0.15 M_{\odot}$ ). Thus the radius of the secondary might be larger, as it would be expected from a lower mass white dwarf given the mass-radius relation. We estimate the secondary to show  $T_{\text{eff}} \sim 4000$  K, given the ratio between fluxes estimated from the light curve.

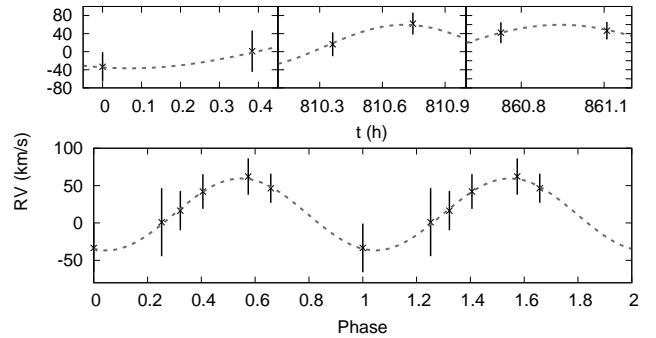


**Figure 11.** Top panel shows the estimated RVs in the three observed epochs for SDSS J004227.73-010634.9. The bottom panel shows a tentative orbital solution, with a 91 min period and  $R^2 = 0.993$ .

## 3.2 Probable (pre-)ELMs

### 3.2.1 J004227.73-010634.9

J0042-0106 was followed up because of the  $\log g > 5.5$  that we obtained by fitting its SDSS spectrum to solar abundance models. Moreover, assuming the object has a main sequence radius, we obtain a distance of over 15 kpc. It was observed in three nights with Gemini South; two spectra were obtained at each night. Although the observed variations are consistent with Gaussian errors, we obtained an orbital solution with  $R^2 = 0.993$  (Fig. 11). The estimated amplitude is  $48 \text{ km s}^{-1}$ , and the period is quite low, of only 91 min. Further observations are required to confirm these findings.

The mass of the primary, given the fit to the SDSS spectrum which resulted on  $T_{\text{eff}} = 8050 \pm 24$  and  $\log g = 5.51 \pm 0.08$ , is  $M = 0.1449 \pm 0.0003 M_{\odot}$ . Assuming the estimated orbital parameters, we obtain the secondary to show  $M_2 > 0.028 M_{\odot}$  (for an inclination of  $60^\circ$ ,  $M_2 = 0.033 M_{\odot}$ , and for  $15^\circ$ ,  $M_2 = 0.22 M_{\odot}$ ). Given the short period, the system would merge in less than a Hubble time ( $\tau_{\text{merge}} < 4.2$  Gyr).



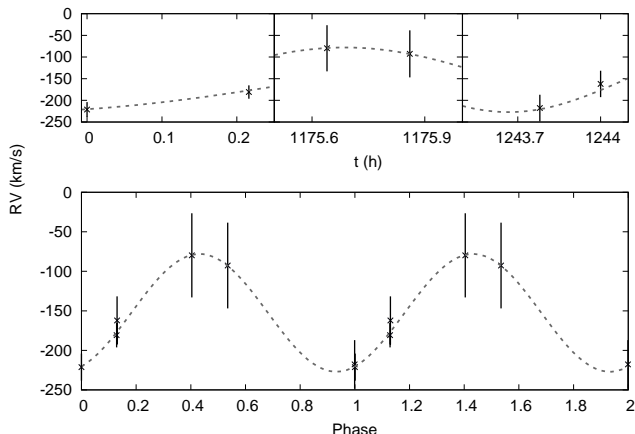


**Figure 12.** Estimated RVs for SDSS J011508.65+005346.1 (top), and the best orbital solution (bottom). The average uncertainty was  $33 \text{ km s}^{-1}$ , much larger than our typical values of  $10\text{--}15 \text{ km s}^{-1}$ , due to the bias issue at GMOS South.

### 3.2.2 J011508.65+005346.1

J0115+0053 also shows  $\log g > 5.5$  in our solar abundance fits to its SDSS spectrum, and  $d > 15 \text{ kpc}$  when a main sequence radius is assumed. Moreover, we found it to be more likely ELM in Pelisoli et al. (2018), given its space motion, colours, and physical parameters. We obtained six spectra at three nights with Gemini. The obtained RVs show real variability only at a 70 per cent confidence level, but we obtained  $R^2 = 0.97$  for the best orbital solution, with  $T = 100 \text{ min}$  and  $K = 74 \text{ km s}^{-1}$  (see Fig. 12). However, all the spectra were affected by the bright columns that appeared at the Gemini South CCD during the end of 2016B, hence the uncertainties in the velocities are larger.

Given the  $T_{\text{eff}} = 8670 \pm 24 \text{ K}$  and the  $\log g = 5.64 \pm 0.08$ , and the hinted RV variability, we propose J0115+0053 is a probable ELM, but we caution that more data is needed to confirm this identification. The evolutionary models give a primary mass of  $0.150 \pm 0.001 M_{\odot}$ , and, assuming the tentative orbital parameters, the minimal secondary mass is  $0.049 M_{\odot}$  ( $M_2 = 0.058 M_{\odot}$  for  $i = 60^\circ$ , and  $M_2 = 0.54 M_{\odot}$  for  $i = 15^\circ$ ), and the merging time is shorter than 3.2 Gyr.

### 3.2.3 J030608.92-001338.9

We found J0306-0013 to be most likely a (pre-)ELM in Pelisoli et al. (2018). It was classified as a sdA in Kepler et al. (2016). We obtained ten spectra over two nights at SOAR. Fitting the combined spectrum to our  $Z = 0.1 Z_{\odot}$  grid, we obtain  $T_{\text{eff}} = 7770 \pm 10 \text{ K}$  and  $\log g = 5.36 \pm 0.04$ , implying  $M = 0.1433 \pm 0.0004 M_{\odot}$ . The Shapiro-Wilk test yields  $p < 0.3$ , suggesting the estimated RVs vary at the 70 per cent confidence level. With only two nights, it is hard to constrain the orbital period. We find two solutions with  $R^2$  differing by less than two per cent for  $T = 28.6 \text{ h}$  and  $T = 13.5 \text{ h}$ , the former with  $K = 186 \text{ km s}^{-1}$ , and the latter with  $K = 88 \text{ km s}^{-1}$ . Both solutions are shown in Fig. 13.

For the 28.6 h period, the secondary has a relatively high minimum mass of  $\sim 1.0 M_{\odot}$ . For any inclination above  $60^\circ$ , the companion would have to be a neutron star. The

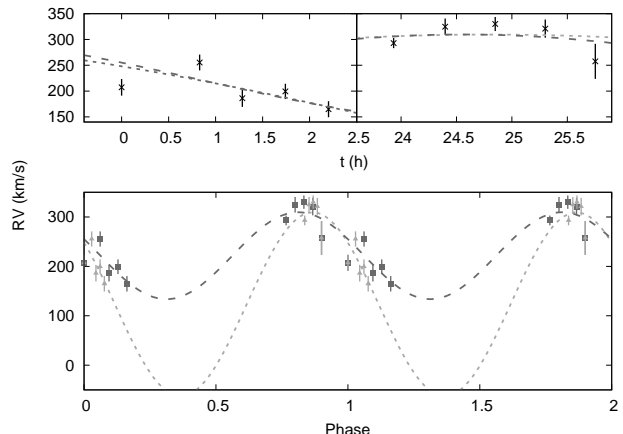


**Figure 13.** The top panel shows the estimated RVs for SDSS J030608.92-001338.9 in the two observed nights. Two orbital solutions are shown: short dashed line (light grey) for the 28.1 h period, and the long dashed line (dark grey) for the 13.1 h period. In the bottom panel, the RVs are phase folded to these two periods, following the same colour code.

merging time for this period is smaller than 546 Gyr. On the other hand, for the 13.5 h period, the minimal mass is  $M_2 > 0.15 M_{\odot}$ , and the merging time is shorter than 320 Gyr.

### 3.2.4 J045515.00-043231.0

J0455-0432 was also found to be most likely a (pre-)ELM in Pelisoli et al. (2018). Eleven spectra were obtained over two nights at SOAR. The estimated RVs suggest variability at 65 per cent confidence level. We obtain a dominant period of 4.1 h, but with a high uncertainty of 3.8 h. We estimate  $K = 60 \pm 24 \text{ km s}^{-1}$ . The orbital solution assuming the 4.1 h period, shown in Fig. 14, gives  $R^2 = 0.89$ .

The SOAR spectrum suggests  $T_{\text{eff}} = 8250 \pm 8 \text{ K}$  and  $\log g = 4.15 \pm 0.03$ . These values are consistent with a pre-ELM of  $M = 0.180 \pm 0.001 M_{\odot}$ , in a binary with an object of minimal mass  $0.061 M_{\odot}$  ( $0.073 M_{\odot}$  for  $i = 60^\circ$ , and  $0.69 M_{\odot}$  for  $i = 15^\circ$ ), which will merge within 25 Gyr.

### 3.2.5 J122911.49-003814.4

The radial velocity we derived for J1229-0038 from its SDSS spectrum was  $472 \pm 3 \text{ km s}^{-1}$ , consistent with the  $465 \pm 5 \text{ km s}^{-1}$  given by the SDSS spectral pipeline fit and close to the escape velocity of the Galaxy. Moreover, a main sequence radius would place it at a distance close to 15 kpc, inconsistent with its proper motion of  $10.2 \pm 1.8 \text{ mas yr}^{-1}$  (Tian et al. 2017). Observing it for two nights at SOAR, we obtained five spectra. Although the Shapiro-Wilk test suggests the variability can be explained by Gaussian noise, we find an orbital solution with  $R^2 = 0.96$ ,  $T = 3 \text{ h}$ , and  $K = 47 \text{ km s}^{-1}$ . We estimate a very high systemic velocity of  $510 \text{ km s}^{-1}$ , consistent with the SDSS spectrum, suggesting the semi-amplitude might actually be higher. More data are needed to constrain the orbit of this object

The fit to its SOAR spectrum gives  $T_{\text{eff}} = 8300 \pm 21 \text{ K}$  and  $\log g = 5.65 \pm 0.06$ , implying a mass  $M = 0.1476 \pm$

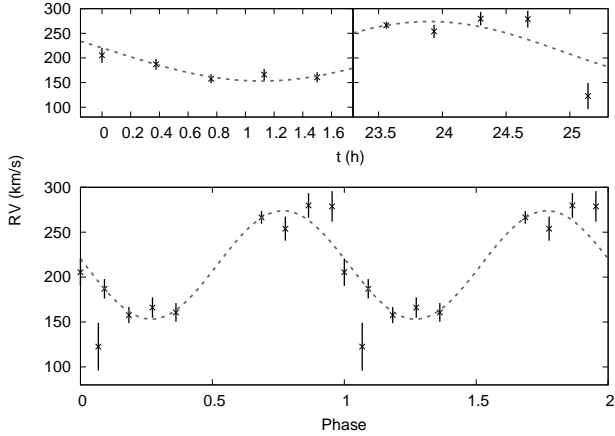


**Figure 14.** Obtained RVs for SDSS J045515.00-043231.0 are shown in the top panel. Bottom panel shows the RVs phase-folded to a 4.1 h period.

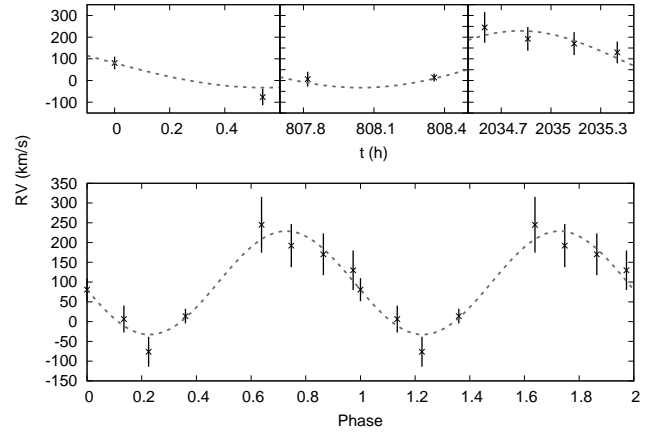


**Figure 16.** Radial velocity estimates (top) and the best orbital solution (bottom) for SDSS J233606.13-102551.5.

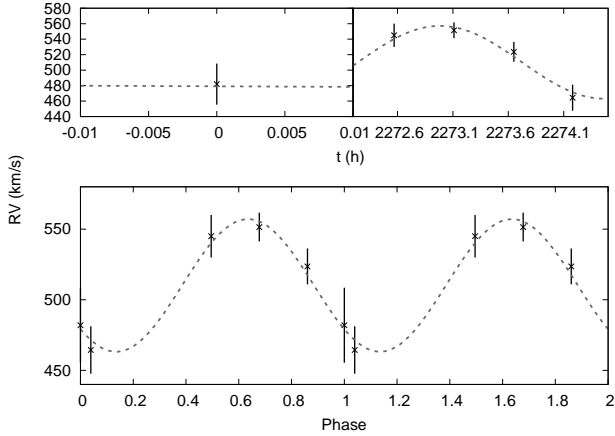


**Figure 15.** Radial velocities (top) and best orbital solution (bottom) for SDSS J122911.49-003814.4. The systemic velocity of over  $500 \text{ km s}^{-1}$  might indicate that the semi-amplitude is much higher than the derived  $47 \text{ km s}^{-1}$ .

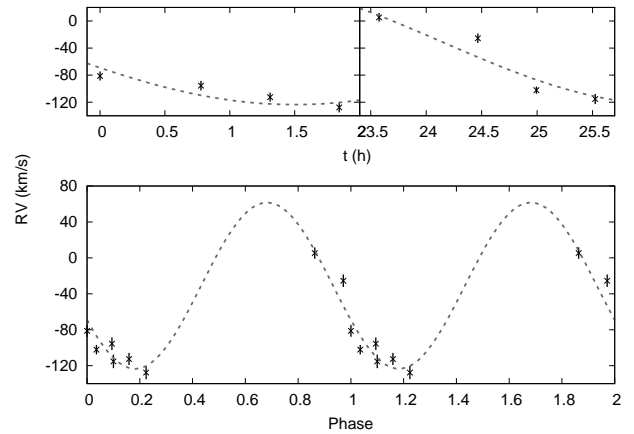


**Figure 17.** The estimated RVs for SDSS J162624.91+162201.5 are shown in the top panel, while the bottom panel shows the velocities phase-folded to the 8.2 h period, together with the orbital solution.

$0.0009 M_{\odot}$  in the models of [Althaus et al. \(2013\)](#). Assuming the obtained orbital parameters are correct, the mass of the companion should be higher than  $M_2 = 0.035 M_{\odot}$ , or equal to  $0.32 M_{\odot}$  for  $i = 15^{\circ}$ . The mass for most probable  $i = 60^{\circ}$  inclination is  $0.042 M_{\odot}$ . The merging time is just above a Hubble time,  $\tau_{\text{merge}} < 20 \text{ Gyr}$ .

### 3.2.6 J233606.13-102551.5

J2336-1025 would be at a distance larger than 26 kpc if it had a main sequence radius. We obtained  $\log g = 5.72 \pm 0.15$  and  $T_{\text{eff}} = 8330 \pm 39 \text{ K}$  from its SDSS spectrum using our solar abundance models. This implies  $M = 0.149 \pm 0.003 M_{\odot}$  and  $R = 0.088 \pm 0.02 R_{\odot}$ . We followed it up for three nights with Gemini South, obtaining six spectra. The RV estimates hint a period of 2.4 h, even though the variability could also be explained by Gaussian uncertainties. The best orbital solution ( $R^2 = 0.92$ ) gives  $K = 131 \text{ km s}^{-1}$  and is shown in Fig. 16. With these orbital parameters, we obtain  $M_2 > 0.12 M_{\odot}$  and  $\tau_{\text{merge}} < 3.73 \text{ Gyr}$ , shorter than a Hubble time.

### 3.2.7 J162624.91+162201.5

We obtained in [Pelisoli et al. \(2018\)](#) that J1626+1622 is most likely a (pre-)ELM. It was followed-up for two nights at SOAR, when we obtained eight spectra. At a 90 per cent confidence level, the detected RV variability cannot be explained by random uncertainty. We estimated a period of  $8.2 \pm 0.1 \text{ h}$  and  $K = 92.6 \pm 19.3 \text{ km s}^{-1}$ , obtaining an orbital solution with  $R^2 = 0.88$ , shown in Fig. 17.

However, J1626+1622 we derived a low  $\log g = 3.83 \pm 0.03$ , with  $T_{\text{eff}} = 7460 \pm 15 \text{ K}$ , from its combined SOAR spectrum. Similar parameters are obtained from the SDSS spectrum. With these parameters, we could only explain it as a pre-ELM in a CNO flash. The time scale of these flashes ranges from  $10^5$  to  $10^6$  years. The estimated physical parameters are consistent with the flashes of a  $M = 0.34 M_{\odot}$  model. Given the estimated orbital parameters,  $M_2 > 0.20 M_{\odot}$  and  $\tau_{\text{merge}} < 32 \text{ Gyr}$ .

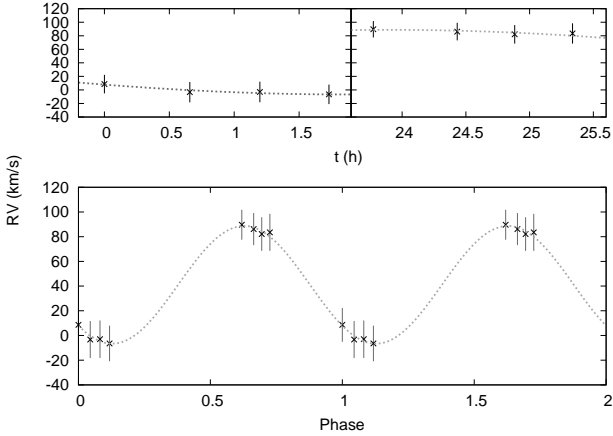


**Figure 18.** The orbital solution for the SOAR data of SDSS J090410.00+034332.9, folded to the 14.7 h period (bottom), and the estimated RVs (top).

### 3.2.8 J090410.00+034332.9

We obtained eight spectra over two nights at SOAR for J0904+0343, given its RV variability in the SDSS subspectra. The normality test gave  $p = 0.006$ , confirming the variability. We estimated a period of  $14.7 \pm 0.3$  h, with a low semi-amplitude of  $47.7 \pm 2.4$  km s<sup>-1</sup>, suggesting either a high-orbital inclination, or that the object is a main sequence binary. The orbital solution, shown in Fig. 18 gives  $R^2 = 0.997$ .

J0904+0343 SOAR spectrum fits  $T_{\text{eff}} = 7680 \pm 20$  and  $\log g = 4.08 \pm 0.05$ , assuming  $0.1 Z_{\odot}$ . This is compatible with a pre-ELM of mass  $0.18 \pm 0.05 M_{\odot}$  given the models of Althaus et al. (2013). However, it could also mean that the object is a binary metal poor F star in the halo. The estimated distance given a main sequence radius is 9 kpc, and the proper motion is quite low and uncertain ( $3.3 \pm 3.1$  mas yr<sup>-1</sup>). The low detected semi-amplitude results on a low minimal mass of  $0.08 M_{\odot}$  assuming a pre-ELM primary, given that the orbit would probably not be edge-on. For a 15° inclination, the mass is about  $1.05 M_{\odot}$ , and for 60°, it is  $0.092 M_{\odot}$ . The merging time would be up to 590 Gyr.

We will be able to estimate the distance for this star and others with the parallax to be released by Gaia, and therefore the difference between our preferred solution as a pre-ELM and a 9 kpc main sequence star will be clear.

### 3.3 No detected variation

Fig. 19 shows the RV estimates for the objects with no statistically significant RV variations, and no good orbital solutions in the probed ranges of periods, described below. We caution that periods as short as 12 min were observed for the known ELMs (Brown et al. 2011b), and theoretical models predict periods of several days (Sun & Arras 2017).

J222009.74-092709.9 was found to be a photometric variable in OPD data (see Fig. 20). Despite its reliable proper motion of  $\mu = 9.6 \pm 1.6$  mas yr<sup>-1</sup>, we did not find it to be most likely ELM in Pelisoli et al. (2018) given its colours. The spectroscopic follow-up revealed no orbital periods in the range  $\sim 20$  min to  $\sim 200$  days. However, we obtain  $\log g = 6.10 \pm 0.02$  and  $T_{\text{eff}} = 8230 \pm 6$  K for the

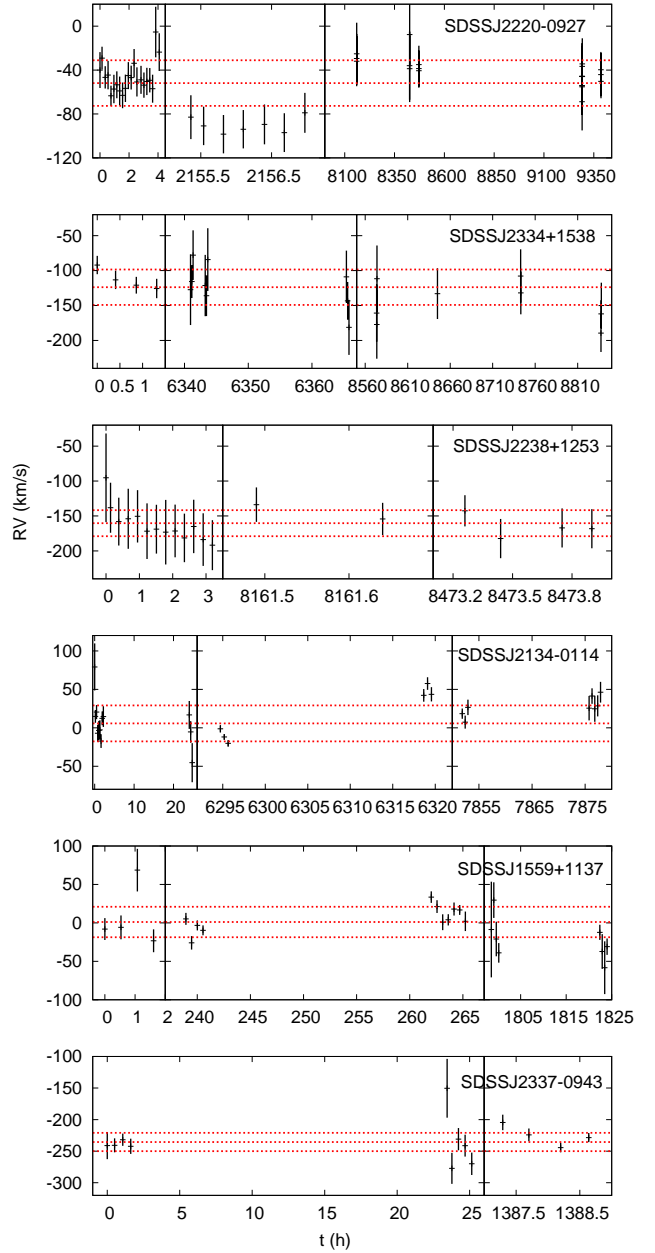


**Figure 19.** Velocities for the six objects observed in multiple epochs, with no statistically detected variation.

SOAR spectra of this object, which not only places it in the region of the known ELMs, but also within the instability strip given by Tremblay et al. (2015), thus justifying the observed photometric variability. We suggest further monitoring of this object should be done to probe shorter and longer orbital periods, as well as further time series photometry to allow an asteroseismological study.

J233403.21+153829.2, J223831.91+125318.3, and J155937.48+113721.9 also have reliable proper motion according to the criteria of Pelisoli et al. (2018) ( $39.1 \pm 1.5$ ,  $13.6 \pm 1.6$ , and  $7.4 \pm 1.8$  mas yr<sup>-1</sup>, respectively, according to Tian et al. 2017), yet they were not found to be most likely ELMs. J1559+1137 has not been previously cited in the literature. Our estimated physical parameters are close

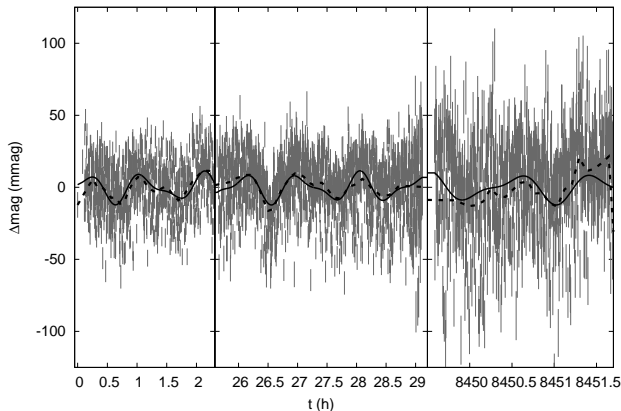


**Figure 20.** OPD light curve for 222009.74-092709.9. Two periods were found above a detection limit of  $4 \langle A \rangle$ , where  $\langle A \rangle$  is the average amplitude of the Fourier transform. The fit to the light curve given these two periods is shown as continuous line. The dashed line shows the smoothed data.

to the main sequence upper limit,  $T_{\text{eff}} = 11880 \pm 41$  K and  $\log g = 4.83 \pm 0.01$ . The lack of RV variation and periods in the range  $\sim 1$  h to  $\sim 40$  days suggests it is either a short period or ELM, or possibly a halo blue straggler star.

J2343+1538 in particular was suggested to be an extremely-metal poor (EMP) star by Aoki et al. (2013). Their adopted physical parameters based on the SEGUE stellar parameter pipeline (SSPP, Lee et al. 2008),  $T_{\text{eff}} = 6500$  K and  $\log g = 4.0$ , agree within external uncertainties with the parameters we estimate from SOAR spectra,  $T_{\text{eff}} = 6710 \pm 17$  K and  $\log g = 4.25 \pm 0.05$ . No periods were found in the  $\sim 24$  min to  $\sim 180$  day range, thus the EMP explanation seems likely, although at odds with the high proper motion.

J2238+1253 was photometrically classified as a horizontal branch (HB) star by Xue et al. (2008). However, given our estimated physical parameters from its SOAR spectrum,  $T_{\text{eff}} = 7870 \pm 9$  K and  $\log g = 5.17 \pm 0.05$ , this classification seems unlikely, considering both the low temperature and high  $\log g$ . We find nonetheless no periods in the range  $\sim 20$  min to  $\sim 180$  days. The object could either be an EMP with an overestimated  $\log g$ , or a single ELM, formed through one of the alternative paths to binary evolution described in the Introduction. *Gaia* parallax will allow us to determine its nature.

J213428.63-011409.3 and J233708.62-094307.0 were both followed up considering the high proper motions ( $> 12$  mas yr $^{-1}$ ) displayed in the catalogue of Munn et al. (2014). However, both values were actually unreliable due to close by sources, and the proper motions given in the recent GPS1 catalogue (Tian et al. 2017) are much smaller and quite uncertain. For J2134-0114, not only no RV variation is found, but the fit to the SOAR spectrum suggests a relatively low  $\log g = 3.76 \pm 0.02$ , and  $T_{\text{eff}} = 12320 \pm 84$  K, placing it above the zero-age horizontal branch (ZAHB). It could thus be a HB star. We cannot, however, discard the possibility that it is a (pre-)ELM in a CNO flash. J2337-0943, on the other hand, lies below the ZAHB, with  $T_{\text{eff}} = 8020 \pm 12$  K and  $\log g = 4.59 \pm 0.06$ . Such parameters are consistent with a  $M = 0.160 \pm 0.004 M_{\odot}$  pre-ELM, but the no detection of orbital periods in the range 1 h to 30 days and the

**Table 2.** Physical properties derived for the objects observed with X-shooter, with models assuming  $Z = 0.1 Z_{\odot}$

SDSS J	$T_{\text{eff}}$ (K)	$\log g$
024932.84-010708.4	$8219 \pm 13$	$4.775 \pm 0.044$
101701.89+070806.8	$8746 \pm 6$	$4.331 \pm 0.020$
112620.47+090145.5	$8467 \pm 7$	$4.640 \pm 0.021$
112616.66-010140.7	$8073 \pm 8$	$4.834 \pm 0.025$
233343.95-001502.0	$8279 \pm 6$	$4.410 \pm 0.016$

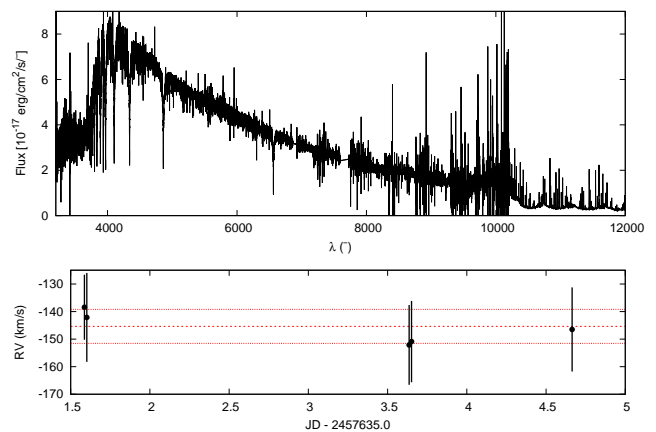


**Figure 21.** The top panel shows the combined X-shooter spectrum for J024932.84-010708.4. No companion can be identified in the red. The bottom panel shows the RVs obtained for the spectra taken at three different nights. The dashed lines show the weighted mean and the  $\pm 1 \sigma$  values.

lack of reliable ( $> 3\sigma$ ) proper motion suggest it could be a metal-poor A/F star instead.

The five objects observed with X-shooter – J024932.84-010708.4, J101701.89+070806.8, J112620.47+090145.5, J112616.66-010140.7, and J233343.95-001502.0 – are shown in Figs. 21 to 25. Their physical properties as estimated from their X-shooter spectra are given in Table 2. Besides no RV variation, it can also be noted that they have no red companions. They all showed  $\log g > 5.5$  in our fit to their SDSS spectra assuming solar abundances. Most show  $\log g \gtrsim 5.5$  also when  $Z = 0.1 Z_{\odot}$  is assumed. Interestingly, the fit to the X-shooter spectra assuming  $Z = 0.1 Z_{\odot}$  suggests a  $\log g$  lower by  $\sim 1$  dex. Possible reasons are discussed in Section 3.4. The obtained parameters and the fact that none shows significant proper motion suggests they could all be metal-poor A/F stars. However, we caution that they are hotter and apparently less metallic than known low-metallicity stars (e.g. Yong et al. 2013).

### 3.4 Spectral fits

Fig. 26 shows the comparison between our fit to SDSS spectra and to spectra obtained as part of this work, with the same grid of models ( $Z = 0.1 Z_{\odot}$ ). The effective temperature seems to agree remarkably well between spectra obtained with different facilities, with average differences of less than 2 per cent. The  $\log g$ , on the other hand, shows a larger spread. Considering the spectra obtained with SOAR,

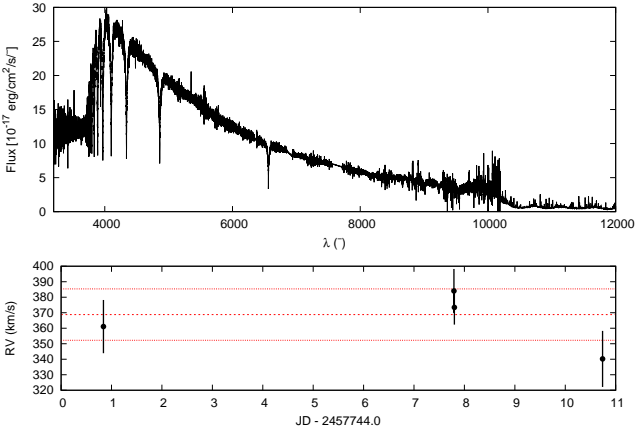


**Figure 22.** Combined X-shooter spectrum for J101701.89+070806.8 (top), and the RVs obtained from each individual spectrum (bottom). The weighted mean and  $\pm 1 \sigma$  values are indicated by the dashed lines.

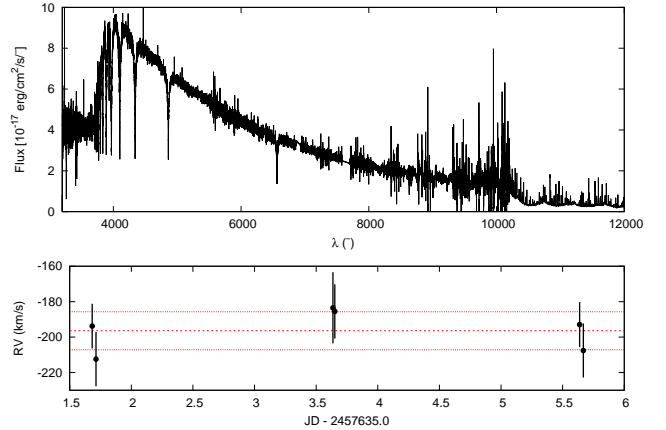


**Figure 25.** Bottom panel shows the RV estimates for J233343.95-001502.0, and the top panels shows the combined Doppler-corrected spectrum for all epochs.

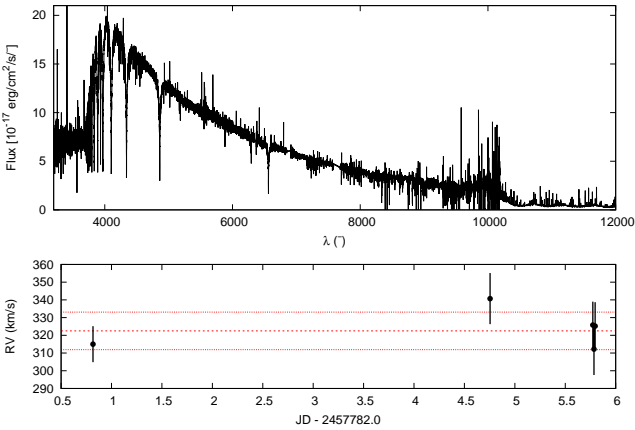


**Figure 23.** The estimate RVs for J112620.47+090145.5 (bottom), obtained from the individual spectrum taken at three different nights. The Doppler-corrected combined spectrum is shown in the top panel.

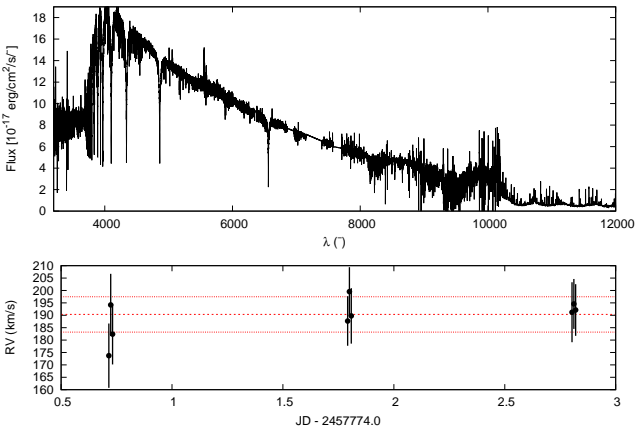


**Figure 24.** X-shooter spectrum (top) and RV estimates (bottom) for J112616.66-010140.7. The RV estimates agree between the three nights.

the average difference to SDSS, considering only objects whose fit is not at the border of our grid, is only about 0.08 dex, hence completely consistent with the uncertainties. However, comparing the four X-shooter spectra to SDSS, we obtain a large difference of  $-0.93$  dex. The grid of models is the same, so the difference cannot be explained by metallicity as suggested by [Brown et al. \(2017\)](#).

The main differences between X-shooter and SDSS/SOAR spectra are the wavelength coverage and the spectral resolution. At low temperatures, the width of the lines is not very sensitive to  $\log g$ , and the  $\log g$  determination depends essentially on flux below 3700 Å. Spectra obtained with the SDSS spectrograph only cover above 3800 Å. More recent spectra obtained with BOSS extend the coverage down to 3600 Å, but usually with low-S/N in this wavelength range. This region is also very sensitive to flux calibration and extinction. Hence  $\log g$  estimates from SDSS spectra might be affected by these uncertainties. We had previously assumed an external 0.25 dex uncertainty ([Pelisoli et al. 2018](#)), but it appears that it might be even larger, up to 0.50 dex. It is important to caution, however, that these four objects were selected on a very large sample, with tens of thousands of sdAs ([Pelisoli et al. 2018](#)), hence we should expect to find several objects with errors of  $2-3 \sigma$ . In short, we cannot assert that this difference between SDSS and X-shooter spectral fits is systematic, as it might result from statistical fluctuations.

The adopted physical parameters for our new and probable (pre-)ELMs are shown in Table 3, as well as their estimated orbital parameters. Fig. 27 is similar to Fig. 1, including these new objects. These additions to the known sample of ELMs improve the comparison between model predictions and observed population, by adding objects both to cool and to low-mass ends of the (pre-)ELM space of physical parameters.

### 3.5 Photometry

Besides J1343+0826 and J2220-0927 described in Sections 3.1.4 and 3.3, we have found five other sdAs to show variability. Pulsation periods and amplitudes for all



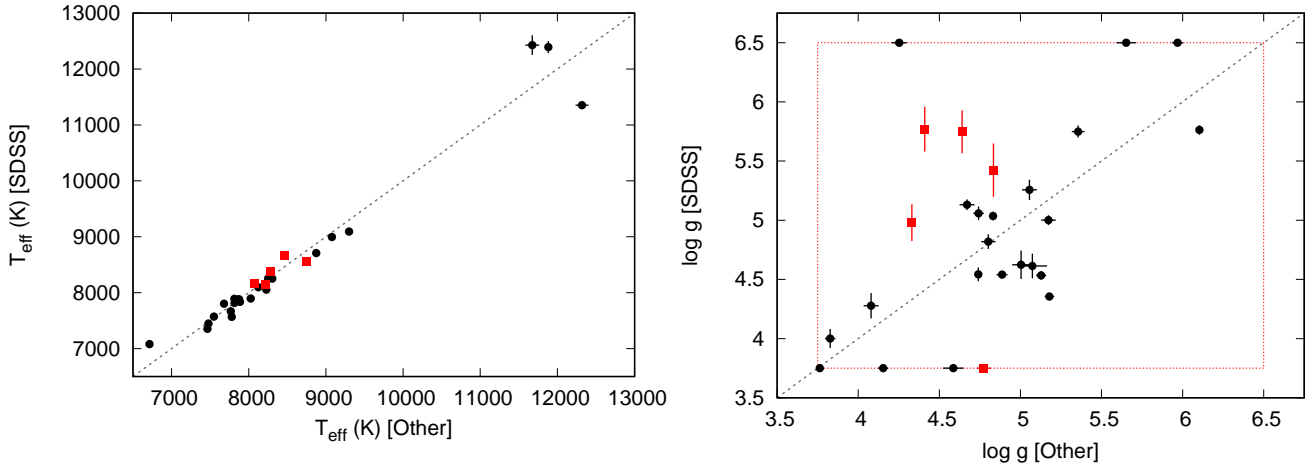


**Figure 26.** Comparison between the physical parameters obtained by fitting SDSS spectra or SOAR/X-shooter spectra (labelled as other). The physical parameters derived from SOAR spectra are shown as black dots, while parameters derived from X-shooter spectra are shown as red squares. There is a very good agreement, to less than 2 per cent, in  $T_{\text{eff}}$  (left). The dashed rectangle in the  $\log g$  panel (right) indicates the border of the model grid. Considering objects within this limits, SOAR and SDSS  $\log g$  show a low average difference of 0.08 dex. The X-shooter spectra suggest a  $\log g$  lower by 0.93 dex, what could be due to the better resolution and larger spectral coverage provided by X-shooter, but could also be explained by statistical fluctuations, as detailed in the text.

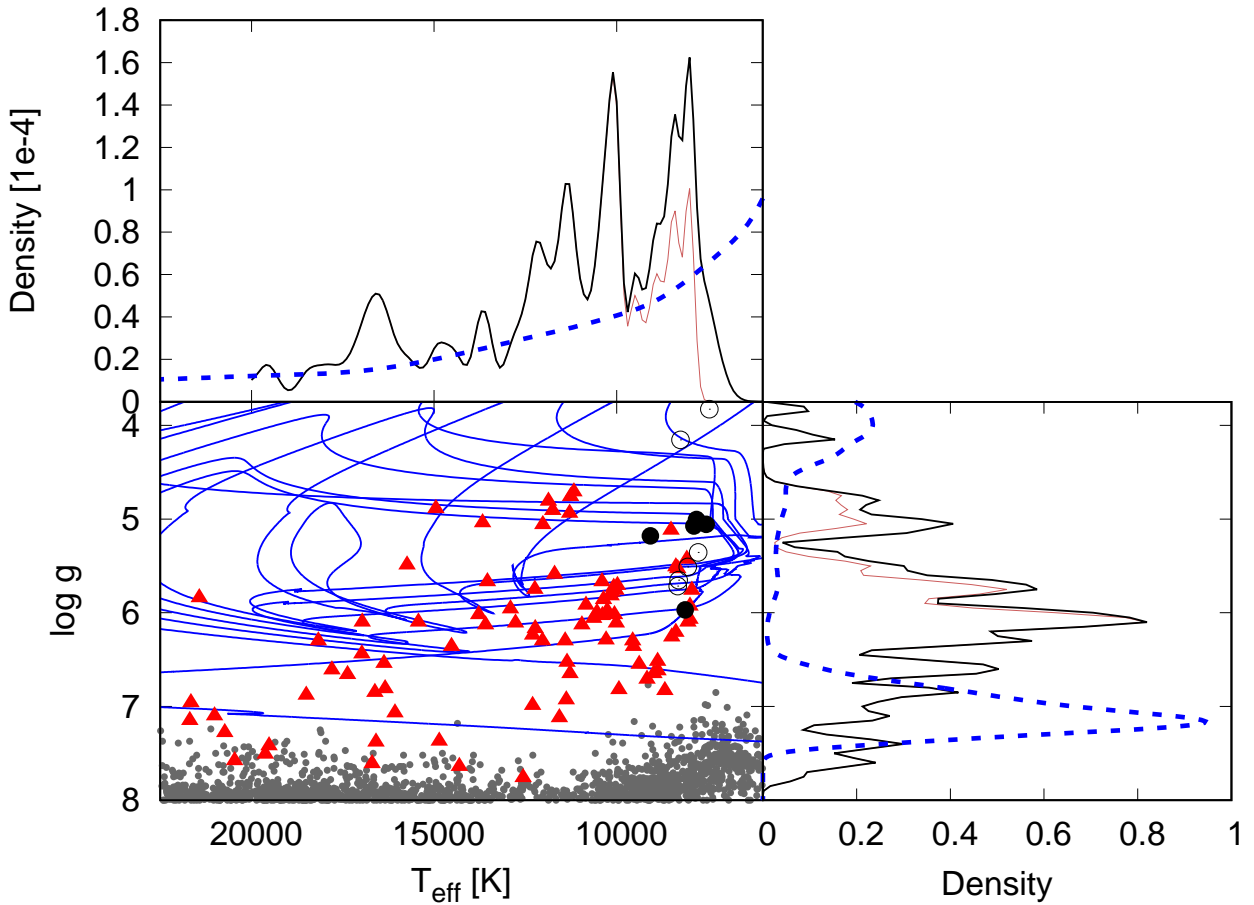


**Figure 27.** Same as Fig. 1, adding the new (pre-)ELMs (filled black circles) and probable (pre-)ELMs (open black circles). The distributions with these added objects are shown in black. Especially in  $T_{\text{eff}}$ , the population seems more similar to the predicted by the models. There are still missing (pre-)ELMs in the lower  $\log g$  end.

**Table 3.** Estimated physical and orbital properties for the new and probable (pre-)ELMs, which are separated by a horizontal line.  $T_{\text{eff}}$  and  $\log g$  were estimated assuming  $Z = 0.1 Z_{\odot}$ . The secondary mass is the lower limit ( $i = 90^{\circ}$ ), and the time for merging is the upper limit. The uncertainties in  $P$  and  $K$  were calculated with a thousand Monte Carlo simulations in PERIOD04.

SDSS J	$T_{\text{eff}}$ (K)	$\log g$	$M$ ( $M_{\odot}$ )	$P_{\text{orb}}$ (h)	$K$ (km/s)	$M_2$ ( $M_{\odot}$ )	$\tau_{\text{merge}}$ (Gyr)
032914.77+003321.8	$9077 \pm 10$	$5.179 \pm 0.029$	$0.1536 \pm 0.0006$	$20.0 \pm 0.1$	$83 \pm 22$	0.17	765
073934.37+172225.5	$7548 \pm 12$	$5.056 \pm 0.046$	$0.1450 \pm 0.0011$	$6.64 \pm 0.03$	$82.6 \pm 6.8$	0.10	68
084034.83+045357.6	$7886 \pm 32$	$5.074 \pm 0.091$	$0.1470 \pm 0.0022$	$8.13 \pm 0.01$	$222 \pm 13$	0.59	28
134336.44+082639.4	$8123 \pm 10$	$5.969 \pm 0.034$	$0.1527 \pm 0.0011$	$24.692 \pm 0.002$	$136.2 \pm 7.0$	0.43	410
142421.30-021425.4	$9299 \pm 11$	$5.128 \pm 0.031$	$0.1558 \pm 0.0008$	$6.3 \pm 0.4$	$80 \pm 22$	0.09	57
205120.67+014554.4	$7813 \pm 12$	$5.004 \pm 0.055$	$0.1476 \pm 0.0014$	$22.9 \pm 0.2$	$138 \pm 14$	0.45	533
092056.09+013114.8	$7478 \pm 13$	$4.802 \pm 0.044$	$0.1492 \pm 0.0014$	$15.742 \pm 0.003$	$75.7 \pm 8.1$	0.09	50
004227.73-010634.9	$8051 \pm 24$	$5.510 \pm 0.081$	$0.1449 \pm 0.0003$	$1.52231 \pm 0.00002$	$48.1 \pm 1.6$	0.14	4.2
011508.65+005346.1	$8673 \pm 24$	$5.641 \pm 0.080$	$0.1499 \pm 0.0011$	$1.678517 \pm 0.000009$	$74.5 \pm 5.5$	0.05	3.1
030608.92-001338.9 <sup>a</sup>	$7768 \pm 10$	$5.356 \pm 0.039$	$0.1433 \pm 0.0004$	$28.6 \pm 1.1$	$186 \pm 61$	1.03	546
				$13.5 \pm 2.3$	$88 \pm 19$	0.15	320
045515.00-043231.0	$8251 \pm 8$	$4.154 \pm 0.031$	$0.1796 \pm 0.0014$	$4.1 \pm 3.8$	$60 \pm 23$	0.06	25
090410.00+034332.9	$7680 \pm 20$	$4.079 \pm 0.046$	$0.1810 \pm 0.0488$	$14.7 \pm 0.3$	$47.7 \pm 2.4$	0.08	590
122911.49-003814.4	$8305 \pm 21$	$5.652 \pm 0.060$	$0.1477 \pm 0.0009$	$2.96 \pm 0.08$	$47 \pm 5.0$	0.04	20
162624.91+162201.5	$7464 \pm 15$	$3.827 \pm 0.032$	$0.3454 \pm 0.0127$	$8.2 \pm 0.1$	$93 \pm 19$	0.20	32
233606.13-102551.5	$8328 \pm 39$	$5.716 \pm 0.147$	$0.1487 \pm 0.0030$	$2.38904 \pm 0.0008$	$131 \pm 11$	0.12	3.7

<sup>a</sup> Two distinct periods are possible with the current data. Parameters for both are shown.

these seven objects are shown in Table 4. Two objects – J073958.57+175834.4 and J075519.92+091511.0 – show large amplitude variations with periods above 2 h. The estimated parameters from SDSS spectra assuming  $Z = 0.1 Z_{\odot}$  are  $T_{\text{eff}} = 36136 \pm 67$  and  $\log g = 6.00 \pm 0.02$  for J0739+1758. For J0755+0915, we could not obtain a good fit with the  $Z = 0.1 Z_{\odot}$  grid — the  $\log g$  is too close to the lower limit of the grid. For solar metallicity, we obtain  $T_{\text{eff}} = 7470 \pm 5$  K and  $\log g = 4.50 \pm 0.04$ . None of these two shows significant proper motion. J0755+0915 could be explained as a metal poor A/F star, but we caution that there is at least one pre-ELM known to show RR Lyrae pulsations (Pietrzyński et al. 2012), given that during the CNO flashes the pre-ELM can reach the RR Lyrae instability strip. J0739+1758 was photometrically selected as a possible AM CVn binary by Carter et al. (2013). However, both the long period and the fact the SDSS spectrum shows no emission lines seem to rule out this possibility. Its temperature places it within the region where subdwarf stars show pulsations (see Fig. 30), hence it could be a new variable subdwarf star. The spectroscopic fit places the object within the domain of V361 Hya stars (first discovered by Kilkeny et al. 1997,  $T_{\text{eff}} > 28000$  K). However, V361 Hya stars usually show  $p$ -mode pulsations with short periods (100–400 s). A few were found to show also  $g$ -modes (e.g. Schuh et al. 2005), but the  $g$ -mode pulsations show low-amplitude, unlike what we found. A photometric fit to this object with fixed  $\log g = 6.0$  suggests a lower temperature of  $T_{\text{eff}} = 21745 \pm 280$ . Our spectral models do not take into account line blanketing by metals or NLTE effects, which are often important for hot subdwarfs (e.g. Nemeth et al. 2014), hence in this case the spectral parameters should be only taken as a rough estimate. The photometric  $T_{\text{eff}}$  places the object in the V1093 Her domain (a class first found by Green et al. 2003). V1093 Her stars show  $g$ -mode pulsations of the order of hours, as we have observed. The amplitude we observed is nonetheless higher than for the known V1093

Her stars. Further data is required to better determine the nature of J0739+1758.

A third object, J075738.94+144827.5 was studied in Sánchez-Arias et al. (submitted to A&A) and found to be more likely a  $\delta$ -Scuti star, given the spacing between periods, a result that should be confirmed by the parallax. Two other new variables, J160040.95+102511.7 and J201757.29-125615.6, are shown in Figs. 28 and 29, respectively. The derived physical parameters for the SDSS spectrum of J1600+1025 assuming  $Z = 0.1 Z_{\odot}$  are  $T_{\text{eff}} = 7816 \pm 10$  K and  $\log g = 4.63 \pm 0.05$ , placing it slightly above the instability strip in Fig. 30. Assuming solar metallicity, the parameters are  $T_{\text{eff}} = 8050 \pm 8$  K and  $\log g = 5.59 \pm 0.03$ , placing it within the instability strip of Tremblay et al. (2015). Its proper motion is  $7.1 \pm 1.2$  mas yr<sup>-1</sup>. For J2017-1256, the derived physical parameters from the SDSS spectra assuming either solar metallicity or  $Z = 0.1 Z_{\odot}$  place it slightly above the instability strip. The  $Z = 0.1 Z_{\odot}$  parameters are  $T_{\text{eff}} = 8138 \pm 9$  K and  $\log g = 5.14 \pm 0.05$ . The proper motion is smaller than 5 mas yr<sup>-1</sup>, with an uncertainty of almost 2 mas yr<sup>-1</sup> (Tian et al. 2017). The estimated  $\log g$  of both objects is too high for  $\delta$ -Scuti stars, which have similar spectral properties to (pre-)ELMs, but show  $\log g < 4.4$  (e.g., Murphy et al. 2015). However, given the uncertainties in  $\log g$  described in Section 3.4, the  $\log g$  could be lower. We obtain a distances of over 3 kpc assuming a main sequence radius, and  $z > 1$  kpc given their relatively high galactic latitude. Unfortunately, the number of periods is insufficient for an asteroseismological analysis, thus conclusions on the nature of these objects require more data.

We have also observed fourteen other objects for at least 2 h, and integration times shorter than 30 s, and found no pulsations. The observing time and obtained detection limits are shown in Table 5. They are shown in Fig. 30 as not observed to vary, but we caution that this does not mean they are not variables. Beating can cause destructive interference and essentially hide the pulsations for hours

**Table 4.** Periods and amplitudes for all objects found to be photometrically variable, as well as  $T_{\text{eff}}$  and  $\log g$  derived from the SDSS spectra (SOAR for J134336.44+082639.4 and J222009.74-092709.9), assuming  $Z = 0.1 Z_{\odot}$ . For J160040.95+102511.7 and J075519.92+091511.0, a good fit is not obtained with  $Z = 0.1 Z_{\odot}$ ; we then assumed solar metallicity.

Object	$T_{\text{eff}}$ (K)	$\log g$	Period (s)	Amplitude (mmag)
J134336.44+082639.4	$8120 \pm 10$	$5.97 \pm 0.03$	$26.2 \pm 2.4$	
J222009.74-092709.9	$8230 \pm 6$	$6.10 \pm 0.02$	$3591.24 \pm 0.03$ $2168.8 \pm 0.2$	$7.9 \pm 0.7$ $3.9 \pm 0.7$
J075738.94+144827.5	$8180 \pm 7$	$4.75 \pm 0.04$	$2437 \pm 15$ $2986 \pm 22$ $2059 \pm 16$ $802 \pm 5$	$3.3 \pm 0.1$ $2.2 \pm 0.1$ $1.7 \pm 0.1$ $0.5 \pm 0.1$
J160040.95+102511.7	$7816 \pm 10$	$4.63 \pm 0.05$	$3849 \pm 57$ $2923 \pm 32$ $2133 \pm 21$	$3.1 \pm 0.2$ $1.4 \pm 0.2$ $1.0 \pm 0.2$
J201757.29-125615.6	$8138 \pm 9$	$5.14 \pm 0.05$	$7171 \pm 49$ $3011 \pm 58$	$9.0 \pm 0.5$ $4.1 \pm 0.5$
J073958.57+175834.4	$36136 \pm 67$	$6.00 \pm 0.02$	$> 11\,000$	$> 40$
J075519.92+091511.0	$7470 \pm 5$	$4.50 \pm 0.04$	$> 7800$	$> 100$

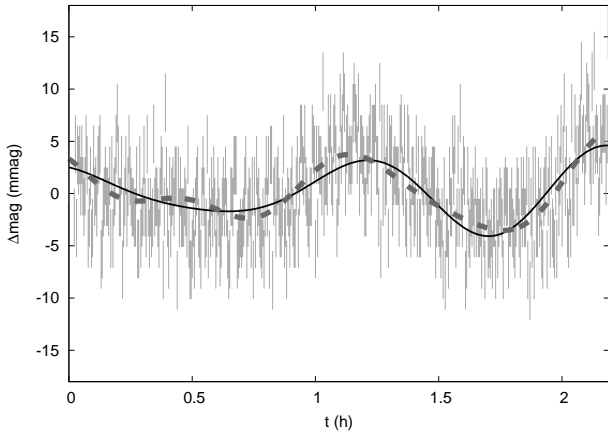


**Figure 28.** SOAR light curve for 160040.95+102511.7. The grey continuous line is a fit considering the two periods above a  $4 \langle A \rangle$ ,  $3849 \pm 57$  s with an amplitude of  $3.1 \pm 0.2$  mmag, and  $2923 \pm 32$  s with  $1.4 \pm 0.2$  mmag. The dashed lined adds a third period, which shows an amplitude larger than  $3.9 \langle A \rangle$ ,  $2133 \pm 21$  s with  $1.0 \pm 0.2$  mmag.

(Castanheira et al. 2007). Moreover, the objects can show pulsations below the detection limit or outside the probed periods.

#### 4 DISCUSSION

With these new pre-ELM and ELM discoveries, we add twelve objects to the  $T_{\text{eff}} < 9000$  K range. With the three confirmed ELMs in this range given in Brown et al. (2016a), we reach of total of fifteen objects, compared to 75 in the  $T_{\text{eff}} > 9000$  K range (73 confirmed binaries of Brown et al. 2016a, plus J032914.77+003321.8 and J142421.30-021425.4, found in this work). This raises the fraction of cool ELMs

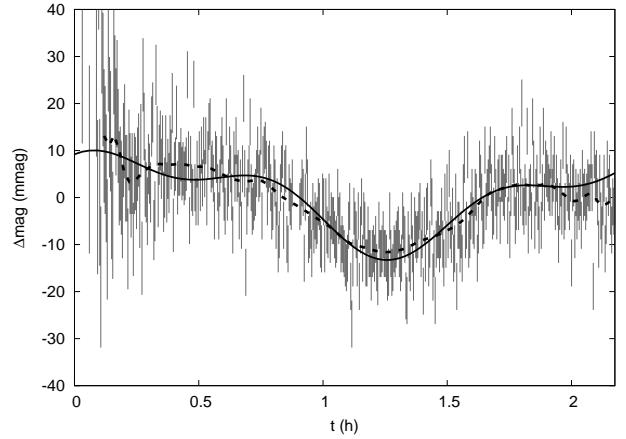


**Figure 29.** SOAR light curve for and best fit (continuous line) for 201757.29-125615.6. We find two periods,  $7171 \pm 49$  s with and amplitude of  $9.0 \pm 0.5$  mmag and  $3011 \pm 58$  s and amplitude of  $4.1 \pm 0.5$  mmag. Here the dashed line is a smoothing of the data.

from 4 per cent to 20 per cent, which is consistent with the predictions by evolutionary models, considering the uncertainties behind the residual burning.

All of our 15 discoveries show  $\log g < 6.0$ . Combined with the 26 objects of the ELM Survey in this range, there are now 41 objects in the low-mass end of the ELM distribution. There are 50 objects with  $\log g > 6.0$ . The fraction is thus close to 1:1; however, the brightness of the lower  $\log g$  objects suggests the fraction could be as high as 100:1 (Pelisoli et al. 2018). Thus, as Fig. 27 already suggested, the population of low-mass objects seems to be missing still. As we considered the estimated  $\log g$  as a selection criterion during most of our follow-up, preferring objects with  $\log g > 5.0$  or even  $> 5.5$ , the fact that this population is not unveiled by our work is not surprising, as there are still thousands of sdAs to be observed. With the upcoming data

**Table 5.** Objects not observed to vary. The physical parameters were estimated from the SDSS spectra assuming  $Z = 0.1 Z_{\odot}$ . For J233625.92+150259.6, we have assumed solar metallicity because no good fit could be obtained with  $Z = 0.1 Z_{\odot}$ .

SDSS J	$T_{\text{eff}}$ (K)	$\log g$	Telescope	Exposure time (h)	$3 \langle A \rangle$
092140.37+004347.9	$7733 \pm 43$	$5.315 \pm 0.179$	SOAR	4.0	5.0
143333.45+041000.8	$8814 \pm 39$	$5.404 \pm 0.157$	SOAR	1.8	7.0
233625.92+150259.6	$8246 \pm 20$	$6.207 \pm 0.061$	OPD	2.7	10.0
112058.97+042012.3	$13840 \pm 265$	$5.147 \pm 0.065$	SOAR	2.4	9.0
204038.41-010215.7	$7886 \pm 19$	$4.833 \pm 0.096$	SOAR	1.6	40.0
			OPD	2.2	6.0
163625.08+113312.4	$8538 \pm 25$	$4.064 \pm 0.060$	OPD	4.4	12.0
110338.46-160617.4	$8275 \pm 10$	$4.734 \pm 0.051$	OPD	5.9	10.0
140353.33+164208.1	$8062 \pm 10$	$5.261 \pm 0.035$	OPD	3.0	4.0
165700.89+130759.6	$8308 \pm 11$	$4.825 \pm 0.047$	SOAR	2.6	25.0
			OPD	5.3	10.0
075133.48+101809.4	$12954 \pm 131$	$3.779 \pm 0.034$	SOAR	2.2	1.5
045001.34-042712.9	$7797 \pm 35$	$4.098 \pm 0.219$	SOAR	3.2	8.0
104522.80-023735.6	$6950 \pm 36$	$4.467 \pm 0.086$	SOAR	2.1	7.0
094144.89+001233.8	$7859 \pm 32$	$4.689 \pm 0.087$	SOAR	2.9	6.0
111041.50+132354.3	$7859 \pm 32$	$4.689 \pm 0.087$	SOAR	3.2	6.0

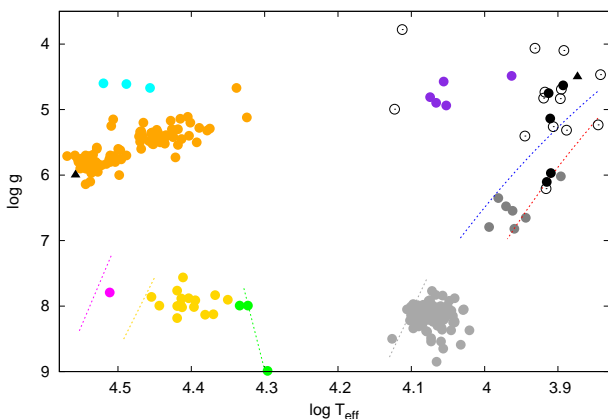


**Figure 30.** Location of the newly detected variables (filled black symbols) in the  $T_{\text{eff}} - \log g$  diagram. The triangles are the two objects with high amplitude pulsations. Open black circles are objects not observed to vary. The hot (blue line) and cool (red line) edges of the ELM instability strip shown as dotted lines were extracted from Tremblay et al. (2015). Other pulsating white dwarfs are shown as in fig. 1 of Córscico & Althaus (2016): pre-ELMVs (purple), ELMVs (dark grey), DAVs (light grey, bottom right), DQVs (green, at  $\log T_{\text{eff}} \sim 4.3$ ), DBVs (yellow), and the only known hot DAV (magenta, bottom left). We have also added the sdV stars from Holdsworth et al. (2017) (orange), and the newly discovered blue large amplitude pulsators (BLAPs, shown in cyan) from Pietrukowicz et al. (2017) as comparison.

release 2 of the *Gaia* missing, finding this population will be a much easier task.

Out of the five observed objects found to be most likely ELM in Pelisoli et al. (2018) (J0115+0053, J0306-0013, J1626+1622, J1343+0826, J0455-0432), one was confirmed as an ELM, and the remaining four were found to be probable ELMs. Four of the objects for which we found no RV variability were also studied in Pelisoli et al. (2018), where a higher probability for the MS channel was obtained. It seems that the probability criteria of Pelisoli et al. (2018)

are a good indication of the nature of the probed sdAs. On the other hand, ten of the objects we followed up spectroscopically were flagged as possible ELMs in the table 1 of Pelisoli et al. (2018) given their  $\log g > 5.5$  estimated from SDSS spectra, but only one was confirmed as ELM (SDSSJ1343+0826), and two others were found to be possible ELMs (SDSSJ0042-0106 and SDSSJ0115+0053). This seems to suggest that the  $\log g$  estimate, especially from SDSS spectra, is not a reliable criteria for selecting ELM candidates. This is in line with our findings described in Section 3.4. Spectral coverage of the  $\lambda < 3700 \text{ \AA}$  region with good S/N seems to be a requirement for a reliable estimate of the  $\log g$  in this  $T_{\text{eff}}$  range. This might also explain the discrepancies found by Brown et al. (2017), but a study with a statistically significant sample is required to confirm this.

None of the newly discovered (pre-)ELMs has a orbital period short enough ( $\lesssim 1 \text{ h}$ ) to be above the predicted detection limit of the upcoming LISA gravitational wave detector. However, such short periods were not probed by our survey, given that most objects were observed with SOAR, a 4.1 m telescope, and required integration times close to 30 min to achieve  $S/N \gtrsim 10$  in the individual spectra. Searching for this shorter periods might be interesting for the objects described Section 3.3, especially J2220-0927, which not only shows  $\log g > 6.0$  in our spectroscopic fit, but also photometric variability with periods in the ELM range.

The objects for which we found no RV variations could alternatively be metal-poor A/F stars in the halo, as already suggested by Brown et al. (2017) as a possible explanation for the sdAs. J2343+1538 in particular seems to be indeed an EMP star, as already suggested by Aoki et al. (2013). The five objects observed with X-shooter, which show no significant proper motion, could also be explained as such. J2134-0114 shows parameters consistent with a HB star, but the nature of the other objects remains puzzling. All show  $g < 20.0$ , therefore they should be included in the DR2 of *Gaia*, making it possible to constrain their radii and determine their nature with certainty. Follow up will still be required for the objects found to be ELMs in order to estimate their orbital parameters, given that *Gaia* will not be able to

resolve binaries with separations below about 20 milliarcsec ( $\sim 2$  AU for a distance of 100 pc).

We have also found seven new photometrically variable stars. J1334+0826 was confirmed as a  $M = 0.15 M_{\odot}$  ELM with time-resolved spectroscopy, so its the eight member of the ELMV class, adding to the seven known pulsating ELMs (Hermes et al. 2012, 2013b,a; Kilic et al. 2015; Bell et al. 2015). We found no RV variations for J2220-0927, but its estimated  $\log g$  and temperature place it inside the instability strip, so it is possibly the ninth member of the class. Time-resolved spectroscopy with larger telescopes, allowing shorter integration times, should be done to probe shorter orbital periods for this object. Two other objects, J1600+1025 and J2017-1256, are also found to show pulsations, and are within the instability ELMV strip given uncertainties. Bell et al. (2017) found three pulsating stars among the objects in the ELM Survey showing no radial velocity variations, suggesting they are related to the sdA population and might be  $\delta$ -Scuti stars with an overestimated  $\log g$ , which might also be the case for these objects. Hence, as we have not obtained time resolved spectroscopy for these two stars, we make no claim about their nature given the uncertainties in the  $\log g$  estimated from SDSS spectra. Recently, Vos et al. (2018) found evidence of a pre-ELM in a long period binary ( $771 \pm 3$  days), likely the result of a merger of the inner binary in a hierarchical triple system. This is also a possible explanation for the systems for which we find no RV variation in short timescales. Another of the variables we discovered, J0739 +1758, seems to be a sdBV, given the  $T_{\text{eff}} > 20000$  K. Finally, J0755+0915 shows high amplitude pulsations similar to RR Lyrae stars. The estimated physical parameters and the low proper motion ( $3.5 \pm 1.7$  mas yr $^{-1}$  according to Tian et al. 2017) are consistent with a halo metal poor F star.

## 5 SUMMARY AND CONCLUSIONS

We present radial velocity estimates and spectral fits for 26 sdAs. We find seven to be new (pre-)ELMs, and further eight others to show most characteristics consistent with (pre-)ELMs, but requiring more data to confirm the detection, hence they are called probable (pre-)ELMs. We perform spectroscopic fits, calculate the best orbital solutions, and provide the physical and orbital parameters for each system (Table 3). With this new detections, the percentage of cool ( $T_{\text{eff}} < 9000$  K) ELMs is raised from 4 to 20 per cent, which is consistent with the predictions of the evolutionary models. Nonetheless there is still a missing population of (pre-)ELMs in the low-mass end, which should be unveiled by *Gaia* DR2. For eleven objects, we find no RV variations, ruling out periods larger than  $\sim 1$  h and shorter than  $\sim 200$  days for most of them. The high rate of identified binaries in the probed sdAs ( $\sim 58$  per cent) suggests that this evolutionary channel indeed plays an important role in explaining the population, as already suggested in Pelisoli et al. (2018).

We have also found the eight member of the ELMV class, J1334+0826. A possible ninth member was also identified, J2220-0927, but its binarity was not confirmed by follow-up time resolved spectroscopy. We found two other sdAs within the ELM instability strip to show pulsations;

however, other objects observed within the instability strip have shown no variability, suggesting the strip might not be pure. This should be further investigated when better estimates on the physical parameters of this objects are available, given the possible uncertainty in SDSS spectra that we have identified, due to the lack of good spectroscopic coverage below 3700 Å.

## ACKNOWLEDGEMENTS

IP, SOK, ADR, and LF acknowledge support from CNPq-Brazil. DK received support from programme Science without Borders, MCIT/MEC-Brazil. IP was also supported by Capes-Brazil under grant 88881.134990/2016-01 and would like to thank Bruno C. Quint for the assistance in observing runs with SOAR.

Based on observations obtained at Observatório do Pico dos Dias / LNA, at the Southern Astrophysical Research (SOAR) telescope, which is a joint project of the Ministério da Ciência, Tecnologia, Inovação e Comunicações (MCTIC) do Brasil, the U.S. National Optical Astronomy Observatory (NOAO), the University of North Carolina at Chapel Hill (UNC), and Michigan State University (MSU), and at the Gemini Observatory and processed using the Gemini IRAF package, which is operated by the Association of Universities for Research in Astronomy, Inc., under a cooperative agreement with the NSF on behalf of the Gemini partnership: the National Science Foundation (United States), the National Research Council (Canada), CONICYT (Chile), Ministerio de Ciencia, Tecnología e Innovación Productiva (Argentina), and Ministério da Ciência, Tecnologia, Inovações e Comunicações (Brasil).

## REFERENCES

- Althaus L. G., Miller Bertolami M. M., Córscico A. H., 2013, *A&A*, **557**, A19
- Altmann M., Roeser S., Demleitner M., Bastian U., Schilbach E., 2017, *A&A*, **600**, L4
- Aoki W., et al., 2013, *AJ*, **145**, 13
- Bell K. J., Kepler S. O., Montgomery M. H., Hermes J. J., Harrold S. T., Winget D. E., 2015, in Dufour P., Bergeron P., Fontaine G., eds, *Astronomical Society of the Pacific Conference Series* Vol. 493, 19th European Workshop on White Dwarfs. p. 217
- Bell K. J., et al., 2017, *ApJ*, **835**, 180
- Bergeron P., Saffer R. A., Liebert J., 1992, *ApJ*, **394**, 228
- Bildsten L., Shen K. J., Weinberg N. N., Nelemans G., 2007, *ApJ*, **662**, L95
- Brown W. R., Geller M. J., Kenyon S. J., 2009, *ApJ*, **690**, 1639
- Brown W. R., Kilic M., Allende Prieto C., Kenyon S. J., 2010, *ApJ*, **723**, 1072
- Brown J. M., Kilic M., Brown W. R., Kenyon S. J., 2011a, *ApJ*, **730**, 67
- Brown W. R., Kilic M., Hermes J. J., Allende Prieto C., Kenyon S. J., Winget D. E., 2011b, *ApJ*, **737**, L23
- Brown W. R., Kilic M., Allende Prieto C., Kenyon S. J., 2012a, *ApJ*, **744**, 142
- Brown W. R., Geller M. J., Kenyon S. J., 2012b, *ApJ*, **751**, 55
- Brown W. R., Kilic M., Allende Prieto C., Gianninas A., Kenyon S. J., 2013, *ApJ*, **769**, 66
- Brown W. R., Geller M. J., Kenyon S. J., 2014, *ApJ*, **787**, 89
- Brown W. R., Gianninas A., Kilic M., Kenyon S. J., Allende Prieto C., 2016a, *ApJ*, **818**, 155



Brown W. R., Kilic M., Kenyon S. J., Gianninas A., 2016b, *ApJ*, **824**, 46

Brown W. R., Kilic M., Gianninas A., 2017, *ApJ*, **839**, 23

Carter P. J., et al., 2013, *MNRAS*, **429**, 2143

Castanheira B. G., et al., 2007, *A&A*, **462**, 989

Clemens J. C., Crain J. A., Anderson R., 2004, in Moorwood A. F. M., Iye M., eds, Proc. SPIE Vol. 5492, Ground-based Instrumentation for Astronomy. pp 331–340, doi:10.1117/12.550069

Córsico A. H., Althaus L. G., 2014, *A&A*, **569**, A106

Córsico A. H., Althaus L. G., 2016, *A&A*, **585**, A1

D’Cruz N. L., Dorman B., Rood R. T., O’Connell R. W., 1996, *ApJ*, **466**, 359

Drake A. J., et al., 2009, *ApJ*, **696**, 870

Drake A. J., et al., 2014, *ApJS*, **213**, 9

Foss D., Wade R. A., Green R. F., 1991, *ApJ*, **374**, 281

Gianninas A., Kilic M., Brown W. R., Canton P., Kenyon S. J., 2015, *ApJ*, **812**, 167

Gimeno G., et al., 2016, in Ground-based and Airborne Instrumentation for Astronomy VI. p. 99082S, doi:10.1117/12.2233883

Green E. M., et al., 2003, *ApJ*, **583**, L31

Hermes J. J., Montgomery M. H., Winget D. E., Brown W. R., Kilic M., Kenyon S. J., 2012, *ApJ*, **750**, L28

Hermes J. J., et al., 2013a, *MNRAS*, **436**, 3573

Hermes J. J., et al., 2013b, *ApJ*, **765**, 102

Holdsworth D. L., Østensen R. H., Smalley B., Telting J. H., 2017, *MNRAS*, **466**, 5020

Hook I. M., Jørgensen I., Allington-Smith J. R., Davies R. L., Metcalfe N., Murowinski R. G., Crampton D., 2004, *PASP*, **116**, 425

Iben Jr. I., Tutukov A. V., 1984, *ApJS*, **54**, 335

Istrate A. G., Marchant P., Tauris T. M., Langer N., Stancliffe R. J., Grassitelli L., 2016, *A&A*, **595**, A35

Kalirai J. S., Hansen B. M. S., Kelson D. D., Reitzel D. B., Rich R. M., Richer H. B., 2008, *ApJ*, **676**, 594

Kepler S. O., et al., 2016, *MNRAS*, **455**, 3413

Kilic M., Brown W. R., Allende Prieto C., Agüeros M. A., Heinke C., Kenyon S. J., 2011, *ApJ*, **727**, 3

Kilic M., Brown W. R., Allende Prieto C., Kenyon S. J., Heinke C. O., Agüeros M. A., Kleinman S. J., 2012, *ApJ*, **751**, 141

Kilic M., Hermes J. J., Gianninas A., Brown W. R., 2015, *MNRAS*, **446**, L26

Kilic M., Munn J. A., Harris H. C., von Hippel T., Liebert J. W., Williams K. A., Jeffery E., DeGennaro S., 2017, *ApJ*, **837**, 162

Kilkenny D., Koen C., O’Donoghue D., Stobie R. S., 1997, *MNRAS*, **285**, 640

Koester D., 2010, Mem. Soc. Astron. Italiana, **81**, 921

Kurtz M. J., Mink D. J., 1998, *PASP*, **110**, 934

Lee Y. S., et al., 2008, *AJ*, **136**, 2022

Lenz P., Breger M., 2005, *Communications in Asteroseismology*, **146**, 53

Liebert J., Bergeron P., Holberg J. B., 2005, *ApJS*, **156**, 47

Lomb N. R., 1976, *Ap&SS*, **39**, 447

Marsh T. R., Dhillon V. S., Duck S. R., 1995, *MNRAS*, **275**, 828

Maxted P. F. L., et al., 2011, *MNRAS*, **418**, 1156

Maxted P. F. L., et al., 2014, *MNRAS*, **437**, 1681

Munn J. A., et al., 2014, *AJ*, **148**, 132

Murphy S. J., Bedding T. R., Niemczura E., Kurtz D. W., Smalley B., 2015, *MNRAS*, **447**, 3948

Nelemans G., Tauris T. M., 1998, *A&A*, **335**, L85

Nemeth P., Østensen R., Tremblay P., Hubeny I., 2014, in van Grootel V., Green E., Fontaine G., Charpinet S., eds, Astronomical Society of the Pacific Conference Series Vol. 481, 6th Meeting on Hot Subdwarf Stars and Related Objects. p. 95 (arXiv:1308.0252)

Palaversa L., et al., 2013, *AJ*, **146**, 101

**Table A1.** Radial velocity data for the targets in Sections 3.1, 3.2, and 3.3. The full table is available in the online version of the paper.

Object	BJD	$RV$ (km/s)	$\sigma_{RV}$ (km/s)
J032914.77+003321.8	2457643.8079	247.306	58.121
	2457643.8153	280.711	19.405
	2457643.8273	264.793	23.636
	2457643.8400	260.744	21.986
	2457643.8521	268.121	37.191
	2457643.8639	203.435	29.317
	2457644.8113	161.653	11.512
	2457644.8232	118.973	14.990
	2457644.8351	139.621	14.224
	2457644.8471	111.585	15.353

Pelisolì I., Kepler S. O., Koester D., 2017, *Open Astronomy*, **26**, 169

Pelisolì I., Kepler S. O., Koester D., 2018, *MNRAS*, **475**, 2480

Pietrukowicz P., et al., 2017, *Nature Astronomy*, **1**, 0166

Pietrzyński G., et al., 2012, *Nature*, **484**, 75

Robinson E. L., Shafter A. W., 1987, *ApJ*, **322**, 296

Romero A. D., Campos F., Kepler S. O., 2015, *MNRAS*, **450**, 3708

Scargle J. D., 1982, *ApJ*, **263**, 835

Schuh S., Huber J., Green E. M., O’Toole S. J., Dreizler S., Heber U., Fontaine G., 2005, in Koester D., Moehler S., eds, Astronomical Society of the Pacific Conference Series Vol. 334, 14th European Workshop on White Dwarfs. p. 530 (arXiv:astro-ph/0411640)

Shapiro S. S., Wilk M. B., 1965, *Biometrika*, **52**, 591

Southworth J., Maxted P. F. L., Smalley B., 2004, *MNRAS*, **351**, 1277

Sun M., Arras P., 2017, preprint, (arXiv:1703.01648)

Tian H.-J., et al., 2017, *ApJS*, **232**, 4

Toonen S., Hollands M., Gänsicke B. T., Boekholt T., 2017, *A&A*, **602**, A16

Tremblay P.-E., Gianninas A., Kilic M., Ludwig H.-G., Steffen M., Freytag B., Hermes J. J., 2015, *ApJ*, **809**, 148

Tremblay P.-E., Cummings J., Kalirai J. S., Gänsicke B. T., Gentile-Fusillo N., Raddi R., 2016, *MNRAS*, **461**, 2100

Vernet J., et al., 2011, *A&A*, **536**, A105

Vos J., Zorotovic M., Vučković M., Schreiber M. R., Østensen R., 2018, *MNRAS*, **477**, 355

Wang B., Han Z., 2009, *A&A*, **508**, L27

Webbink R. F., 1984, *ApJ*, **277**, 355

Woosley S. E., Heger A., 2015, *ApJ*, **810**, 34

Xue X. X., et al., 2008, *ApJ*, **684**, 1143

Yong D., et al., 2013, *ApJ*, **762**, 26

Zacharias N., Finch C., Frouard J., 2017, *AJ*, **153**, 166

Zhang X., Jeffery C. S., 2012, *MNRAS*, **419**, 452

Zhang X., Hall P. D., Jeffery C. S., Bi S., 2017, *ApJ*, **835**, 242

## APPENDIX A: RADIAL VELOCITY DATA

This paper has been typeset from a  $\text{\TeX}/\text{\LaTeX}$  file prepared by the author.